Improved search for $B^0\_s - \bar{B}^0\_s$ oscillations

A. Heister, S. Schael, R. Barate, I. de Bonis, D. Decamp, C. Goy, J.P. Lees, E. Merle, M.N. Minard, B. Pietrzyk, et al.

EUROPEAN ORGANIZATION FOR NUCLEAR RESEARCH (CERN)

CERN-EP/2002-016
February 7, 2002

Improved search for $\mathbf{B_s^0 - \overline{B}_s^0}$ oscillations

The ALEPH Collaboration[1]

Abstract

An improved search for B_s^0 oscillations is performed in the ALEPH data sample collected during the first phase of LEP, and reprocessed in 1998. Three analyses based on complementary event selections are presented. First, decays of B_s^0 mesons into hadronic flavour eigenstates are fully reconstructed. This selection yields a small sample of candidates with excellent decay length and momentum resolution and high average B_s^0 purity. Semileptonic decays with a reconstructed D_s^- meson provide a second sample with larger statistics, high average B_s^0 purity, but a poorer momentum and decay length resolution due to the partial decay reconstruction. Finally, semileptonic b-hadron decays are inclusively selected and yield the data sample with the highest sensitivity to B_s^0 oscillations, as the much higher statistics compensate for the low average B_s^0 purity and poorer time resolution. A lower limit is set at $\Delta m_s > 10.9\,\mathrm{ps}^{-1}$ at 95% C.L., significantly lower than the expected limit of $15.7\,\mathrm{ps}^{-1}$.

(Submitted to The European Physical Journal C)

[1]See next pages for the list of authors.

The ALEPH Collaboration

A. Heister, S. Schael

Physikalisches Institut das RWTH-Aachen, D-52056 Aachen, Germany

R. Barate, I. De Bonis, D. Decamp, C. Goy, J.-P. Lees, E. Merle, M.-N. Minard, B. Pietrzyk

Laboratoire de Physique des Particules (LAPP), IN^{2}P^3-CNRS, F-74019 Annecy-le-Vieux Cedex, France

G. Boix,[24] S. Bravo, M.P. Casado, M. Chmeissani, J.M. Crespo, E. Fernandez, M. Fernandez-Bosman, Ll. Garrido,[15] E. Graugés, M. Martinez, G. Merino, R. Miquel,[27] Ll.M. Mir,[27] A. Pacheco, H. Ruiz

Institut de Física d'Altes Energies, Universitat Autònoma de Barcelona, E-08193 Bellaterra (Barcelona), Spain[7]

A. Colaleo, D. Creanza, M. de Palma, G. Iaselli, G. Maggi, M. Maggi, S. Nuzzo, A. Ranieri, G. Raso,[23] F. Ruggieri, G. Selvaggi, L. Silvestris, P. Tempesta, A. Tricomi,[3] G. Zito

Dipartimento di Fisica, INFN Sezione di Bari, I-70126 Bari, Italy

X. Huang, J. Lin, Q. Ouyang, T. Wang, Y. Xie, R. Xu, S. Xue, J. Zhang, L. Zhang, W. Zhao

Institute of High Energy Physics, Academia Sinica, Beijing, The People's Republic of China[8]

D. Abbaneo, P. Azzurri, O. Buchmüller,[25] M. Cattaneo, F. Cerutti, B. Clerbaux, H. Drevermann, R.W. Forty, M. Frank, F. Gianotti, T.C. Greening,[29] J.B. Hansen, J. Harvey, D.E. Hutchcroft, P. Janot, B. Jost, M. Kado,[31] P. Mato, A. Moutoussi, F. Ranjard, L. Rolandi, D. Schlatter, O. Schneider,[2] G. Sguazzoni, W. Tejessy, F. Teubert, A. Valassi, I. Videau, J. Ward

European Laboratory for Particle Physics (CERN), CH-1211 Geneva 23, Switzerland

F. Badaud, A. Falvard,[22] P. Gay, P. Henrard, J. Jousset, B. Michel, S. Monteil, J-C. Montret, D. Pallin, P. Perret

Laboratoire de Physique Corpusculaire, Université Blaise Pascal, IN^{2}P^3-CNRS, Clermont-Ferrand, F-63177 Aubière, France

J.D. Hansen, J.R. Hansen, P.H. Hansen, B.S. Nilsson

Niels Bohr Institute, DK-2100 Copenhagen, Denmark[9]

A. Kyriakis, C. Markou, E. Simopoulou, A. Vayaki, K. Zachariadou

Nuclear Research Center Demokritos (NRCD), GR-15310 Attiki, Greece

A. Blondel,[12] G. Bonneaud, J.-C. Brient, A. Rougé, M. Rumpf, M. Swynghedauw, M. Verderi, H. Videau

Laboratoire de Physique Nucléaire et des Hautes Energies, Ecole Polytechnique, IN^{2}P^3-CNRS, F-91128 Palaiseau Cedex, France

V. Ciulli, E. Focardi, G. Parrini

Dipartimento di Fisica, Università di Firenze, INFN Sezione di Firenze, I-50125 Firenze, Italy

A. Antonelli, M. Antonelli, G. Bencivenni, F. Bossi, P. Campana, G. Capon, V. Chiarella, P. Laurelli, G. Mannocchi,[5] F. Murtas, G.P. Murtas, L. Passalacqua, M. Pepe-Altarelli[4]

Laboratori Nazionali dell'INFN (LNF-INFN), I-00044 Frascati, Italy

A. Halley, J.G. Lynch, P. Negus, V. O'Shea, C. Raine,[32] A.S. Thompson

Department of Physics and Astronomy, University of Glasgow, Glasgow G12 8QQ,United Kingdom[10]

S. Wasserbaech

Department of Physics, Haverford College, Haverford, PA 19041-1392, U.S.A.

R. Cavanaugh, S. Dhamotharan, C. Geweniger, P. Hanke, V. Hepp, E.E. Kluge, A. Putzer, H. Stenzel, K. Tittel, M. Wunsch[19]

Kirchhoff-Institut für Physik, Universität Heidelberg, D-69120 Heidelberg, Germany[16]

R. Beuselinck, D.M. Binnie, W. Cameron, P.J. Dornan, M. Girone,[1] N. Marinelli, J.K. Sedgbeer, J.C. Thompson[14]

Department of Physics, Imperial College, London SW7 2BZ, United Kingdom[10]

V.M. Ghete, P. Girtler, E. Kneringer, D. Kuhn, G. Rudolph

Institut für Experimentalphysik, Universität Innsbruck, A-6020 Innsbruck, Austria[18]

E. Bouhova-Thacker, C.K. Bowdery, A.J. Finch, F. Foster, G. Hughes, R.W.L. Jones, M.R. Pearson, N.A. Robertson

Department of Physics, University of Lancaster, Lancaster LA1 4YB, United Kingdom[10]

K. Jakobs, K. Kleinknecht, G. Quast,[6] B. Renk, H.-G. Sander, H. Wachsmuth, C. Zeitnitz

Institut für Physik, Universität Mainz, D-55099 Mainz, Germany[16]

A. Bonissent, P. Coyle, O. Leroy, P. Payre, D. Rousseau, M. Talby

Centre de Physique des Particules, Université de la Méditerranée, IN^{2}P^3-CNRS, F-13288 Marseille, France

F. Ragusa

Dipartimento di Fisica, Università di Milano e INFN Sezione di Milano, I-20133 Milano, Italy

A. David, H. Dietl, G. Ganis,[26] K. Hüttmann, G. Lütjens, W. Männer, H.-G. Moser, R. Settles, W. Wiedenmann, G. Wolf

Max-Planck-Institut für Physik, Werner-Heisenberg-Institut, D-80805 München, Germany[16]

J. Boucrot, O. Callot, M. Davier, L. Duflot, J.-F. Grivaz, Ph. Heusse, A. Jacholkowska,[30] J. Lefrançois, J.-J. Veillet, C. Yuan

Laboratoire de l'Accélérateur Linéaire, Université de Paris-Sud, IN^{2}P^3-CNRS, F-91898 Orsay Cedex, France

G. Bagliesi, T. Boccali, L. Foà, A. Giammanco, A. Giassi, F. Ligabue, A. Messineo, F. Palla, G. Sanguinetti, A. Sciabà, P. Spagnolo, R. Tenchini,[1] A. Venturi,[1] P.G. Verdini, Z. Xie

Dipartimento di Fisica dell'Università, INFN Sezione di Pisa, e Scuola Normale Superiore, I-56010 Pisa, Italy

G.A. Blair, G. Cowan, M.G. Green, T. Medcalf, A. Misiejuk, J.A. Strong, P. Teixeira-Dias,
Department of Physics, Royal Holloway & Bedford New College, University of London, Egham, Surrey TW20 OEX, United Kingdom[10]

R.W. Clifft, T.R. Edgecock, P.R. Norton, I.R. Tomalin
Particle Physics Dept., Rutherford Appleton Laboratory, Chilton, Didcot, Oxon OX11 OQX, United Kingdom[10]

B. Bloch-Devaux, P. Colas, S. Emery, W. Kozanecki, E. Lançon, M.-C. Lemaire, E. Locci, P. Perez, J. Rander, J.-F. Renardy, A. Roussarie, J.-P. Schuller, J. Schwindling, A. Trabelsi,[21] B. Vallage

CEA, DAPNIA/Service de Physique des Particules, CE-Saclay, F-91191 Gif-sur-Yvette Cedex, France[17]

N. Konstantinidis, A.M. Litke, G. Taylor

Institute for Particle Physics, University of California at Santa Cruz, Santa Cruz, CA 95064, USA[13]

C.N. Booth, S. Cartwright, F. Combley,[32] M. Lehto, L.F. Thompson

Department of Physics, University of Sheffield, Sheffield S3 7RH, United Kingdom[10]

K. Affholderbach,[28] A. Böhrer, S. Brandt, C. Grupen, A. Ngac, G. Prange, U. Sieler

Fachbereich Physik, Universität Siegen, D-57068 Siegen, Germany[16]

G. Giannini

Dipartimento di Fisica, Università di Trieste e INFN Sezione di Trieste, I-34127 Trieste, Italy

J. Rothberg

Experimental Elementary Particle Physics, University of Washington, Seattle, WA 98195 U.S.A.

S.R. Armstrong, K. Berkelman, K. Cranmer, D.P.S. Ferguson, Y. Gao,[20] S. González, O.J. Hayes, H. Hu, S. Jin,

J. Kile, P.A. McNamara III, J. Nielsen, Y.B. Pan, J.H. von Wimmersperg-Toeller, W. Wiedenmann, J. Wu, Sau Lan Wu, X. Wu, G. Zobernig

Department of Physics, University of Wisconsin, Madison, WI 53706, USA[11]

G. Dissertori

Institute for Particle Physics, ETH Hönggerberg, 8093 Zürich, Switzerland.

[1]Also at CERN, 1211 Geneva 23, Switzerland.
[2]Now at Université de Lausanne, 1015 Lausanne, Switzerland.
[3]Also at Dipartimento di Fisica di Catania and INFN Sezione di Catania, 95129 Catania, Italy.
[4]Now at CERN, 1211 Geneva 23, Switzerland.
[5]Also Istituto di Cosmo-Geofisica del C.N.R., Torino, Italy.
[6]Now at Institut für Experimentelle Kernphysik, Universität Karlsruhe, 76128 Karlsruhe, Germany.
[7]Supported by CICYT, Spain.
[8]Supported by the National Science Foundation of China.
[9]Supported by the Danish Natural Science Research Council.
[10]Supported by the UK Particle Physics and Astronomy Research Council.
[11]Supported by the US Department of Energy, grant DE-FG0295-ER40896.
[12]Now at Departement de Physique Corpusculaire, Université de Genève, 1211 Genève 4, Switzerland.
[13]Supported by the US Department of Energy, grant DE-FG03-92ER40689.
[14]Supported by the Leverhulme Trust.
[15]Permanent address: Universitat de Barcelona, 08208 Barcelona, Spain.
[16]Supported by the Bundesministerium für Bildung, Wissenschaft, Forschung und Technologie, Germany.
[17]Supported by the Direction des Sciences de la Matière, C.E.A.
[18]Supported by the Austrian Ministry for Science and Transport.
[19]Now at SAP AG, 69185 Walldorf, Germany.
[20]Also at Department of Physics, Tsinghua University, Beijing, The People's Republic of China.
[21]Now at Département de Physique, Faculté des Sciences de Tunis, 1060 Le Belvédère, Tunisia.
[22]Now at Groupe d'Astroparticules de Montpellier, Université de Montpellier II, 34095, Montpellier, France
[23]Also at Dipartimento di Fisica e Tecnologie Relative, Università di Palermo, Palermo, Italy.
[24]Now at McKinsey and Compagny, Avenue Louis Casal 18, 1203 Geneva, Switzerland.
[25]Now at SLAC, Stanford, CA 94309, U.S.A.
[26]Now at INFN Sezione di Roma II, Dipartimento di Fisica, Universitá di Roma Tor Vergata, 00133 Roma, Italy.
[27]Now at LBNL, Berkeley, CA 94720, U.S.A.
[28]Now at Skyguide, Swissair Navigation Services, Geneva, Switzerland.
[29]Now at Honeywell, Phoenix AZ, U.S.A.
[30]Also at Groupe d'Astroparticules de Montpellier, Université de Montpellier II, 34095, Montpellier, France.
[31]Now at Fermilab, PO Box 500, MS 352, Batavia, IL 60510, USA.
[32]Deceased.

1 Introduction

The measurement of the $B_s^0 - \overline{B}_s^0$ oscillation frequency is one of the major goals of B physics. The frequency is proportional to the mass difference between the B_s^0 mass eigenstates, Δm_s. Within the Standard Model framework, a measurement of the ratio $\Delta m_s/\Delta m_d$ (Δm_d being the mass difference in the $B^0 - \overline{B}^0$ system) would allow the ratio of Cabibbo-Kobayashi-Maskawa matrix elements $|V_{ts}/V_{td}|$ to be extracted [1]. No experiment has yet been able to resolve B_s^0 oscillations. Lower limits have been set on the frequency, and their combination yields $\Delta m_s > 14.6$ ps^{-1} at 95% C.L. [2].

Three event samples are selected to study B_s^0 oscillations. The first selection aims at the full reconstruction of flavour-specific B_s^0 hadronic decays, such as $B_s^0 \to D_s^- \pi^+$[1]. The other two exploit semileptonic decays of B_s^0 mesons, one with the reconstruction of $D_s^- \ell^+$ pairs, and the other in an inclusive manner. The three analyses have different and complementary strengths. Their results are combined to obtain the final ALEPH results on B_s^0 oscillations.

The analysis based on fully reconstructed B_s^0 candidates is presented for the first time in this paper. The small branching ratios into hadronic final states result in the smallest of the three selected data samples (about 80 candidates). However, because of the high B_s^0 purity of this sample (more than 80% in some channels) and the excellent momentum and decay length resolutions achieved, its sensitivity to B_s^0 oscillations becomes relevant in the high frequency range. The analysis of $D_s^- \ell^+$ pairs presented here is an upgrade of that described in Ref. [3]. The sample analysed consists of about 300 fully reconstructed D_s^- candidates paired with oppositely charged leptons. The B_s^0 purity of this sample, more than 40% on average, and good decay length resolution, partially compensate for the small statistics. The inclusive semileptonic analysis is an upgrade of that in Ref. [4]. This selection provides the largest data sample (about 74 000 candidates), and yields the highest sensitivity to B_s^0 oscillations at all frequencies, despite the lower average B_s^0 purity and poorer proper-time resolution.

Details of the improvements developed for both upgraded analyses are given in the relevant sections throughout the paper. The LEP 1 data were reprocessed using a refined version of the reconstruction algorithms. The main improvements are related to track reconstruction accuracy and particle identification efficiency, both important for the analyses presented here.

The paper is organized as follows. A brief description of the ALEPH detector is given in Section 2, followed by details of the data and simulated samples used by the three analyses. A discussion of the issues common to all B_s^0 oscillation analyses is presented in Section 3. The three following sections (4, 5, and 6) are devoted to the three analyses. Each of these sections starts with a description of the data selection, followed by the B_s^0 oscillations results and consistency checks. The combined results are given in Section 7.

2 Detector and data samples

The ALEPH detector and its performance during the LEP 1 data taking are described in detail elsewhere [5, 6], and only a brief account is given here. Charged particles are tracked in a two-layer silicon vertex detector with double-sided readout ($r\,\phi$ and z), surrounded by a cylindrical drift chamber and a large time projection chamber (TPC). The three tracking devices together

[1] Charge conjugate modes are implied throughout the paper.

measure up to 33 space points along the particle trajectories and give a three-dimensional impact parameter resolution of $(25 + 95/p)\,\mu$m (with the particle momentum p in GeV/c). These detectors are immersed in a 1.5 T axial magnetic field provided by a superconducting solenoidal coil, which results in a transverse momentum resolution $\sigma_{p_{\mathrm{T}}}/p_{\mathrm{T}} = 6 \times 10^{-4}\, p_{\mathrm{T}} \oplus 5 \times 10^{-3}$ (with p_{T} in GeV/c). The TPC also allows particle identification to be performed through the measurement of energy loss by the specific ionization, $\mathrm{d}E/\mathrm{d}x$. Estimators χ_π and χ_{K} are defined as the difference between the expected and the measured ionization loss for the given particle hypothesis, divided by the expected resolution. A kaon/pion separation in excess of two standard deviations is achieved for charged particles with momentum greater than 2 GeV/c. A finely segmented electromagnetic calorimeter (ECAL) of lead/wire-chamber sandwich construction surrounds the TPC. The ECAL is used to identify electrons by their characteristic longitudinal and transverse shower development. Muons are identified by their penetration pattern in the hadron calorimeter (HCAL), and additional three-dimensional coordinates measured in two layers of external muon chambers help in resolving the remaining ambiguities. The almost $4\,\pi$ solid angle coverage of the detector and its fine granularity provide good resolution on the measurement of the missing energy from undetected particles.

The three analyses presented in this paper use approximately four million hadronic Z decays recorded by the ALEPH detector from 1991 to 1995 at centre-of-mass energies close to the Z mass peak. The data were reprocessed in 1998 with improved reconstruction algorithms. In particular, the uncertainty on the TPC z coordinate was reduced by a factor of two and the particle identification ($\mathrm{d}E/\mathrm{d}x$ measurement) was improved and made available for all reconstructed tracks with the combination of pulse height data from the TPC pads with that from the wires [7]. For the analysis based on full reconstruction of hadronic $\mathrm{B_s^0}$ decays, the data taken at the Z peak for calibration purposes during the LEP 2 phase (about 400 000 hadronic events) are also used. The three analyses use hadronic Z decays selected as described in Ref. [8].

Monte Carlo events, simulated with GEANT [9] for the detector response, were used to study both the signal and the background for each analysis. The simulation is based on JETSET [10] with parameters tuned to reproduce inclusive particle spectra and event shape distributions [11], as well as heavy flavour decay properties [12]. Two event samples were used by the three analyses: about eight million hadronic events, and about five million Z decays into $\mathrm{b\overline{b}}$. Specific samples were also used by each of the three analyses, (*i*) about 20 000 events containing one of the hadronic decay modes considered in the analysis of fully reconstructed $\mathrm{B_s^0}$ final states; (*ii*) about 100 000 events containing signal and cascade decays ($\mathrm{b} \to \mathrm{D_s^{\pm}\,D\,X}$, with $\mathrm{D} \to \ell\,\mathrm{X}$) for each of the channels used in the analysis of the $\mathrm{D_s^-}\,\ell^+$ final states; and (*iii*) about one million events containing one direct semileptonic $\mathrm{B_s^0}$ decay. In all simulated samples the $\mathrm{B_s^0}$ oscillation frequency is fixed at $\Delta m_{\mathrm{s}}^{\mathrm{MC}} = 14\,\mathrm{ps}^{-1}$.

3 Issues common to the B_s^0 oscillation analyses

The probability density functions for the proper decay time t of B_s^0 mesons, which either do or do not change flavour between production and decay, are given by

$$\begin{aligned} \mathcal{P}_{B_s^0 \to \overline{B}_s^0}(t) &= \Gamma_s \frac{e^{-\Gamma_s t}}{2} [1 - \cos(\Delta m_s t)] \equiv \mathcal{P}_s^{\rm m}(t) , \\ \mathcal{P}_{B_s^0 \to B_s^0}(t) &= \Gamma_s \frac{e^{-\Gamma_s t}}{2} [1 + \cos(\Delta m_s t)] \equiv \mathcal{P}_s^{\rm u}(t) , \end{aligned} \tag{1}$$

where the effects of CP violation and a possible width difference between the B_s^0 mass eigenstates, $\Delta\Gamma_s$, have been neglected. In both cases, the probability densities follow an exponential decay modulated by an oscillatory term, the frequency of which is proportional to the mass difference Δm_s between the two B_s^0 mass eigenstates. The effect of a nonzero $\Delta\Gamma_s$ is considered as a source of systematic uncertainty (Sections 4.8.1, 5.4.1 and 6.5.1).

Two pieces of information are needed to reconstruct the expressions in Eq. 1: (*i*) the proper time of the B_s^0 decay candidate; and (*ii*) whether or not the B_s^0 meson flavour changes between production and decay. As explained in Section 3.2, the latter point cannot be unambiguously determined on an event-by-event basis.

3.1 Proper-time measurement

The proper time is obtained from the measured decay length l and the reconstructed momentum p of the B_s^0 meson as

$$t = \frac{l\, m}{p} , \tag{2}$$

where m is the B_s^0 meson mass.

The decay length of the B_s^0 meson is measured as the distance between the primary vertex, the point at which the e^+e^- interaction takes place, and the secondary vertex, the point at which the meson decays. The primary vertex is reconstructed for each event as described in Ref. [7]. The secondary vertex is determined with different methods depending on the event selection (Sections 4.6, 5.2 and 6.1.1). The decay length uncertainty σ_l is estimated from the primary and secondary vertex fits, and therefore available event by event. The use of an event-by-event σ_l instead of the average resolution improves the sensitivity to B_s^0 oscillations, in particular at high frequency.

The B_s^0 meson momentum measurement also depends on the event selection (Sections 4.6, 5.2 and 6.2). When the decay is exclusively reconstructed, the momentum is determined with excellent precision as the sum of the momenta of all the decay products. In the case of semileptonic decays, a fraction of the B_s^0 meson momentum is carried by at least one neutrino which escapes undetected. The neutrino momentum is estimated from the requirement of energy and momentum conservation in the event. The B_s^0 momentum is evaluated as the sum of the lepton and the reconstructed charm-candidate momenta, complemented with this neutrino momentum estimate. The resolution in this case is dominated by the resolution on the missing energy, in particular when the D_s^- is fully reconstructed.

The proper-time resolution can be expressed as a function of the decay length and momentum uncertainties (σ_l and σ_p, assumed to be uncorrelated) as

$$\sigma_t = \sqrt{\left(\frac{m}{p}\,\sigma_l\right)^2 + \left(t\,\frac{\sigma_p}{p}\right)^2} \ . \tag{3}$$

The second term of Eq. 3 is proportional to the measured proper time itself. In the case of B_s^0 mesons, the period of the oscillation is much smaller than the lifetime. The sensitivity for partially reconstructed B_s^0 decays comes therefore mostly from short lived mesons, for which the contribution of the momentum resolution to σ_t is small.

The effect of the proper-time resolution on the sensitivity of a B_s^0 oscillation analysis increases strongly with the oscillation frequency tested.

3.2 Flavour tagging

The flavour of the B_s^0 meson (i.e. its particle/antiparticle state) needs to be determined both at production and decay to assign a probability to each B_s^0 candidate of having mixed or not. The combined mistag probability reduces the sensitivity to oscillations, independently of the frequency tested.

3.2.1 Final-state tag

Two different techniques are used in this paper for the final-state (decay) flavour determination. In the case of fully reconstructed B_s^0 decays, all decay products are identified. There is therefore no ambiguity on the final-state flavour. For the two analyses based on semileptonic decays, the sign of the electric charge of the lepton is used as a tag. For the $D_s^- \ell^+$ selection, signal candidates have always a correct tag by construction. For the inclusive semileptonic selection, the nonzero mistag probability is due mainly to $b \to c \to \ell$ cascade decays. It is estimated event by event as described in Section 6.1.3. A mistag probability for the background is also evaluated from simulated events.

3.2.2 Initial-state tag

The flavour at production is determined from the combination of two independent pieces of information, coming from each hemisphere of the event (defined with respect to a plane perpendicular to the thrust axis). The hemisphere which contains (or is opposite to) the B_s^0 candidate is referred to as the same-side (opposite-side) hemisphere. As the Z decays into $b\overline{b}$, the flavour of the b hadron in the opposite-side hemisphere is anti-correlated with that of the B_s^0 at production. Particles in the same-side hemisphere produced close to the B_s^0 meson have their charge correlated to its flavour at production.

- **Opposite side**
  The information from the opposite-side hemisphere is treated in the same manner for the three analyses of this paper, with the charge tag described in Refs. [13, 14]. A neural network is trained on generic b hemispheres to separate tracks originating from the primary and secondary vertices. A weight which gives the probability to come from the secondary vertex is computed for each track and used to build charge variables. Charge estimators

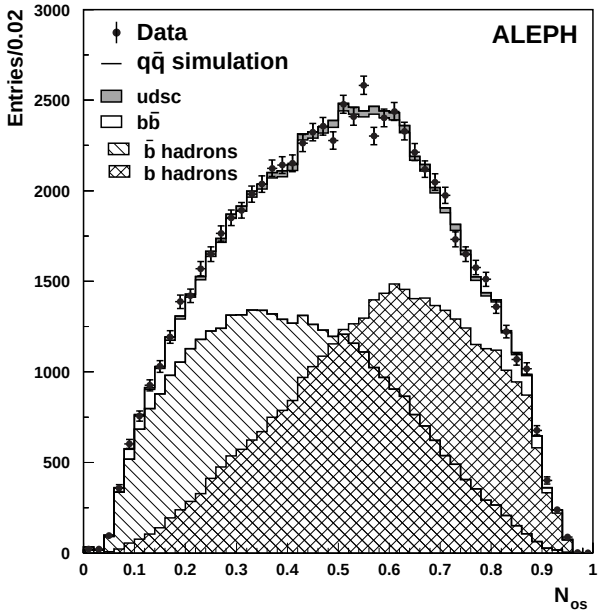

Figure 1: The opposite-side tagging variable, $N_{\rm os}$ (inclusive semileptonic sample), in the data (dots with error bars) and in the simulation (histograms). The shaded area labelled "udsc" corresponds to hemispheres with no b hadron.

such as jet charges, secondary and primary vertex charges, presence and charge of a lepton or a kaon, etc., are combined with a neural network to obtain a single opposite-side tagging variable. The separation between b- and $\overline{\rm b}$-hadron hemispheres obtained with this variable is shown in Fig. 1 for the selected inclusive semileptonic sample (chosen for illustration because of its large statistics).

- **Same side**

  The same side initial-state flavour is determined similarly for the three analyses. The method described here applies to the fully reconstructed $\rm B_s^0$ and the $\rm D_s^- \ell^+$ analyses; the differences for the inclusive semileptonic analysis are discussed in Section 6.3. A *wide* b jet, defined so as to contain all $\rm B_s^0$ meson decay products and the fragmentation particles closest in phase space to the $\rm B_s^0$ meson, is obtained using the JADE algorithm [15], with a large $y_{\rm cut}$ of 0.02. The $\rm B_s^0$ decay products are excluded, and the remaining particles are used to construct charge estimators. When a charged kaon is produced in the fragmentation of the b quark into a $\rm B_s^0$ meson, the charge of this kaon carries information about the flavour of the $\rm B_s^0$ produced. A neural network is trained on simulated events to identify the best fragmentation kaon candidate. Only tracks belonging to the wide jet with an impact parameter significance with respect to the primary vertex smaller than five are considered for the training. The discrimination between kaons and pions is achieved by combining four variables: the track momentum, the pseudo-rapidity with respect to the $\rm B_s^0$ direction, the $\rm d{\it E}/d{\it x}$ estimator $\chi_{\rm K}$, and the $\rm B_s^0$ momentum, that is correlated with the discriminating power of the other three variables. The neural network output, signed with the charge of the kaon candidate, is taken as the charge estimator. In addition, three jet

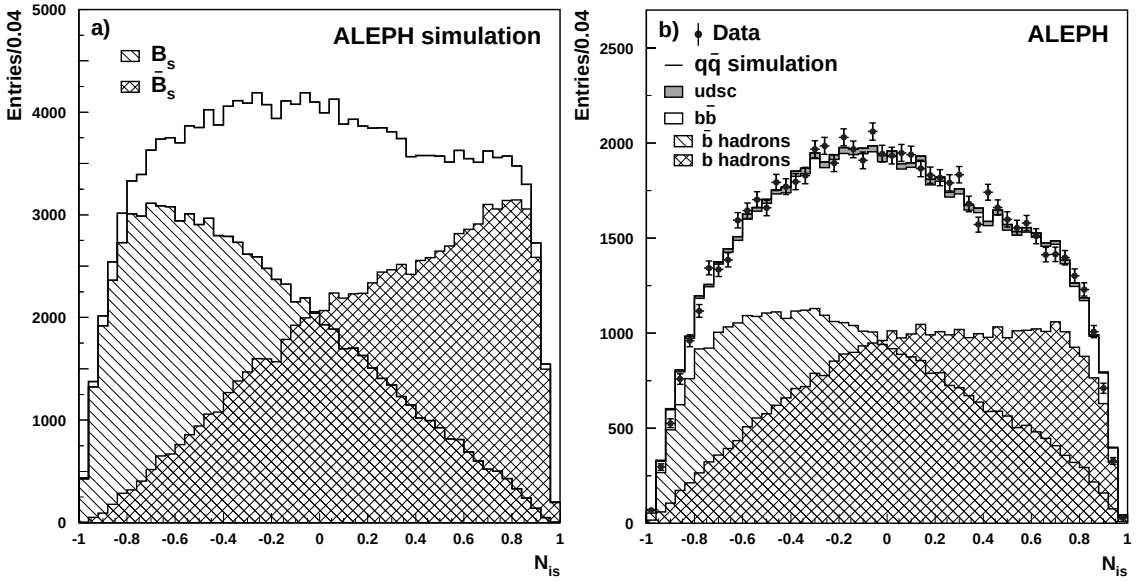

Figure 2: Initial-state tagging variable N_{is} a) for simulated signal events, and b) for all selected events (inclusive semileptonic sample).

charge variables are defined, with momentum-weighting parameter $\kappa = 0$, 0.5 and 1.

- **Additional variables**
  To take advantage of the b forward-backward asymmetry at the Z peak [14], the cosine of the angle of the B_s^0 with respect to the initial electron direction ($\cos\theta_{B_s^0}$) is also used as a global flavour estimator. Other variables are used, not discriminant by themselves, but correlated with the charge-tagging power of the above listed, namely the measured B_s^0 candidate momentum, and the charged particle multiplicity in the jet. Similarly, the spread of weights of the tracks in the opposite-side hemisphere controls the performance of the opposite-side neural network.

The opposite-side variable, the same-side estimators and the additional variables are combined in a final neural network to obtain the initial-state tag. The separation achieved between initially produced B_s^0 and $\overline{B}_s^0$ is shown in Fig. 2a for simulated signal events, and in Fig. 2b for the selected data and simulated hadronic events, for the inclusive semileptonic event sample.

Simulated events are used to parametrize, as a function of the initial-state tagging variable, the probability that a B_s^0 candidate changes flavour between the production and decay time. For signal events the dependence is found to be linear without offset. The event-by-event probability is then used in the oscillation fit to gain statistical power with respect to the use of the average probability.

The effective mistag is defined as the average mistag probability that would result in the same statistical power if the event-by-event probability were not used (the other "effective" variables used throughout the paper are defined in a similar manner). The average initial-state mistag probability for simulated events is evaluated to be about 27%, while the effective mistag probability is about 24% for the three analyses. The performance of the flavour tagging is

different for each background component and therefore parametrized separately for the various components in each of the analyses. The use of neural networks to combine the flavour tagging variables gives improved performance with respect to the two previously published analyses [3, 4].

3.3 Determination of the purity

The statistical power of an event sample for a measurement of the B_s^0 oscillation frequency is proportional to the B_s^0 purity of the sample. For the three analyses, a variable is built to discriminate the B_s^0 signal from each of the background sources. The probability of each candidate to originate from any of the sample components is evaluated as a function of this discriminant variable, and is used in the oscillation fit. An effective B_s^0 purity is defined to quantify the increase in the analysis sensitivity. Each of the three analyses has a specific treatment of the sample composition, the corresponding details are found in Sections 4.5, 5.3 and 6.4.

3.4 The B_s^0 oscillation fit

A B_s^0 signal likelihood function for the three analyses is constructed from the analytical proper-time probability density function. The analytical function $\mathcal{P}_s$ (Eq. 1) is folded with experimental effects (proper-time resolution, reconstruction efficiency and mistag probability). The background components are treated in a different manner for each of the analyses (Sections 4.8, 5.4 and 6.5). The probability density function for each background component is taken wherever possible as an analytical form folded with the experimental effects, as for the B_s^0 signal, or otherwise directly parametrized from the simulation. The unbinned likelihood function for each B_s^0 candidate i therefore reads

$$L_i \;=\; \sum_j^{N_{\rm comp}} f_j^i \left[(1-\eta_j^i)\, \mathcal{P}_j^{\rm u}(t^i) \;+\; \eta_j^i\, \mathcal{P}_j^{\rm m}(t^i) \right] \;, \tag{4}$$

where $N_{\rm comp}$ is the total number of components in the sample (signal and background), f_j^i is the probability that the candidate i originate from component j, η_j^i is the probability that the candidate change flavour between production and decay time if it originates from component j, and $\mathcal{P}_j^{\rm u\,(m)}(t^i)$ is the probability density of the decay proper time for unmixed (mixed) candidates in sample component j folded with all experimental effects. The global likelihood function is obtained as the product of the individual L_i of all candidates.

The proper-time resolution function is written as

$$\mathrm{Res}(t,t_0) \;=\; \sum_j \sum_k f_{l_j} f_{p_k} \frac{1}{\sqrt{2\,\pi}\;\sigma_{t_{jk}}} \exp\left[-\frac{1}{2} \left(\frac{t-t_0}{\sigma_{t_{jk}}} \right)^2 \right] \;, \tag{5}$$

where $\sigma_{t_{jk}}^2 \;=\; (\sigma_{l_j}\, m/p)^2 \,+\, (t\,\delta_{p_k})^2$, t_0 and t are the true and reconstructed proper time respectively, σ_{l_j} and δ_{p_k} are the decay length and relative momentum resolutions, and the sum is made over the Gaussian components that describe these resolutions.

The amplitude method [16, 17] is used to study B_s^0 oscillations as it facilitates the combination of oscillation analyses including the effects of systematic uncertainties. An amplitude $\mathcal{A}$ is

introduced, multiplying the oscillating term of the probability density functions for unmixed and mixed $\mathrm{B_s^0}$ mesons, which then become

$$\mathcal{P}_{\mathrm{s}}^{\mathrm{u,m}}(t) = \frac{\Gamma_{\mathrm{s}}\, e^{-\Gamma_{\mathrm{s}} t}}{2} \left[1 \pm \mathcal{A} \cos(\omega t)\right] . \tag{6}$$

The negative log-likelihood is minimized with respect to $\mathcal{A}$ so that the amplitude is measured for any value of the test frequency ω, with its uncertainty $\sigma_{\mathcal{A}}$. The value $\mathcal{A} = 0$ is expected far below the true oscillation frequency, and $\mathcal{A} = 1$ is expected at $\omega = \Delta m_{\mathrm{s}}$. Frequencies for which $\mathcal{A} + 1.645\,\sigma_{\mathcal{A}} < 1$ are excluded at 95% C.L. The lower limit expected for an infinite oscillation frequency is given by the frequency for which $1.645\,\sigma_{\mathcal{A}} = 1$.

To quantify the effects of systematic uncertainties on the measured amplitude spectra, the relevant physics input variables and detector-related parameters are varied by their estimated uncertainty. As a change in any parameter can result not only in a shift of the fitted amplitude value but also a change in the statistical uncertainty, the following procedure is adopted to quote a total systematic uncertainty which combines correctly both effects. Many toy Monte Carlo experiments are generated in which all the parameters, for which a systematic uncertainty has been assigned, are randomly sampled according to their value and uncertainty. Based on the shift of the fitted amplitude and change of statistical uncertainty observed in the data when each parameter is varied, a distribution for the resulting amplitude is obtained for the toy experiments. The spread of this distribution, at each test frequency, is taken as the combined total uncertainty.

4 Fully reconstructed hadronic analysis

The $\mathrm{B_s^0}$ mesons are selected in the fully hadronic decay modes

$$\mathrm{B_s^0} \to \mathrm{D_s^{(*)-}}\,\pi^+, \quad \mathrm{B_s^0} \to \mathrm{D_s^{(*)-}}\,\mathrm{a_1^+}, \quad \mathrm{B_s^0} \to \mathrm{D_s^{(*)-}}\,\rho^+ \ ,$$

where $\mathrm{D_s^{*-}} \to \mathrm{D_s^-}\gamma$. Only hadronic decays of the $\mathrm{D_s^-}$

$$\mathrm{D_s^-} \to \phi\,\pi^-, \quad \mathrm{D_s^-} \to \mathrm{K^{*0}\,K^-}, \quad \mathrm{D_s^-} \to \mathrm{K_S^0\,K^-} \ ,$$

are considered.

The $\mathrm{K_S^0}$, ϕ, $\mathrm{K^{*0}}$, $\mathrm{a_1^+}$, ρ^0 and ρ^+ candidates are reconstructed in the charged decay modes $\mathrm{K_S^0} \to \pi^+\,\pi^-$, $\phi \to \mathrm{K^+\,K^-}$, $\mathrm{K^{*0}} \to \mathrm{K^+}\,\pi^-$, $\mathrm{a_1^+} \to \rho^0\,\pi^+$, $\rho^0 \to \pi^+\pi^-$, and $\rho^+ \to \pi^+\pi^0$. All charged particles used for the decay reconstruction are required to have a measured $\mathrm{d}E/\mathrm{d}x$ within three standard deviations of that expected for the pion or kaon hypothesis.

The decay modes consisting only of charged particles are the easiest to reconstruct and are discussed first (Sections 4.1 to 4.3). Modes with photons or neutral pions are discussed in Section 4.4.

4.1 The $\mathrm{D_s^-}$ selection

A common approach to the $\mathrm{D_s^-}$ reconstruction is used for the decay modes $\mathrm{D_s^-} \to \phi\,\pi^-$ and $\mathrm{D_s^-} \to \mathrm{K^{*0}\,K^-}$. The neutral daughter of the $\mathrm{D_s^-}$ ($\phi \to \mathrm{K^+\,K^-}$, $\mathrm{K^{*0}} \to \mathrm{K^+}\,\pi^-$) is reconstructed

as a pair of oppositely charged particles with an opening angle less than 90°. The mass of the reconstructed ϕ has to be within $\pm 9\,\mathrm{MeV}/c^2$ of the nominal ϕ mass and that of the reconstructed K^{*0} within $\pm 50\,\mathrm{MeV}/c^2$ of the nominal K^{*0} mass. A third track is then combined with each of the selected pairs to form a three-prong D_s^- decay. The tracks are fitted to a common vertex and, if the mass of the reconstructed D_s^- is within $\pm 30\,\mathrm{MeV}/c^2$ of the nominal mass, it is added as a constraint and the vertex refitted. The probability of the D_s^- vertex fit is required to be greater than 1%. The reconstructed ϕ and K^{*0} (D_s^-) mesons must have momenta greater than $3\,\mathrm{GeV}/c$ ($5\,\mathrm{GeV}/c$). The decay of the pseudoscalar meson D_s^- into a vector meson (ϕ or K^{*0}) and a pseudoscalar meson (π^-) follows a distribution proportional to $\cos^2\lambda$, where λ is the helicity angle. This angle is defined as that between the π^- (K^-) from the D_s^- and one of the ϕ (K^{*0}) daughters in the ϕ (K^{*0}) rest frame. The combinatorial background is reduced with the requirement $|\cos\lambda| > 0.4$.

For $\mathrm{D}_\mathrm{s}^- \to \mathrm{K}_\mathrm{S}^0\,\mathrm{K}^-$ decays, the K_S^0 is reconstructed as described in Ref. [6]. The K_S^0 momentum is required to be greater than $1\,\mathrm{GeV}/c$ and its decay length has to be greater than 4 cm to reject combinatorial background. The K_S^0 is then combined with a charged kaon with momentum greater than $1\,\mathrm{GeV}/c$, to form the D_s^- candidate. To identify the kaon from the D_s^- decay, it is required that $\chi_\mathrm{K} + \chi_\pi < 1.6$. The combination is retained if the $\mathrm{K}_\mathrm{S}^0\,\mathrm{K}^-$ invariant mass is within $\pm 30\,\mathrm{MeV}/c^2$ of the nominal D_s^- mass. Finally the D_s^- vertex is formed with the procedure outlined above for the other two decay modes.

4.2 The a_1^+ selection

For the reconstruction of the $\mathrm{a}_1^+ \to \rho^0\,\pi^+ \to \pi^-\pi^+\pi^+$ decays, the momenta of the pion candidates are required to be greater than $0.5\,\mathrm{GeV}/c$ and those of the reconstructed ρ^0 and a_1^+ to be greater than $1\,\mathrm{GeV}/c$. Three pion candidates, two of which give an invariant mass within $\pm 150\,\mathrm{MeV}/c^2$ of the nominal ρ^0 mass, are required to form a common vertex with a fit probability greater than 1%, and to have an invariant mass within $\pm 300\,\mathrm{MeV}/c^2$ of the nominal a_1^+ mass.

4.3 Reconstruction of $\mathrm{D}_\mathrm{s}^-\pi^+$ and $\mathrm{D}_\mathrm{s}^-\mathrm{a}_1^+$ final states

Selected D_s^- candidates are combined with a π^+ or an a_1^+ candidate to form a B_s^0 meson. Only B_s^0 candidates with a vertex fit probability greater than 1% are kept. The D_s^- vertex must be found downstream of the B_s^0 vertex. The selected π^+ and at least one of the a_1^+ decay products must be reconstructed with at least one VDET hit in either projection. The angle α between the B_s^0 flight direction (determined from the primary vertex and the reconstructed B_s^0 vertex) and the B_s^0 momentum direction (reconstructed with the decay particle momenta) is required to satisfy $\cos\alpha > 0.95$.

The B_s^0 momentum is required to be greater than $20\,\mathrm{GeV}/c$ ($25\,\mathrm{GeV}/c$) in the $\mathrm{D}_\mathrm{s}^-\pi^+$ ($\mathrm{D}_\mathrm{s}^-\mathrm{a}_1^+$) channel. The data sample is further enriched in b-hadron decays by demanding that the reconstructed B_s^0 decay length be greater than three times its estimated uncertainty. To reduce combinatorial background, only the candidate with the largest B_s^0 decay length significance is retained.

The average reconstructed B_s^0 mass resolution in the different decay modes ranges from $17\,\mathrm{MeV}/c^2$ to $25\,\mathrm{MeV}/c^2$, as estimated from simulated signal events. Candidates with a mass

Table 1: Event selection efficiencies for each channel in the invariant mass region $\pm 70\,\mathrm{MeV}/c^2$ around the nominal $\mathrm{B_s^0}$ mass. The uncertainties are about 1% absolute.

Channel	Efficiency (%)
$\mathrm{B_s^0} \to \mathrm{D_s^-}\,\pi^+\,(\phi\,\pi^-)$	19
$\mathrm{B_s^0} \to \mathrm{D_s^-}\,\pi^+\,(\mathrm{K^{*0}\,K^-})$	14
$\mathrm{B_s^0} \to \mathrm{D_s^-}\,\pi^+\,(\mathrm{K_S^0\,K^-})$	11
$\mathrm{B_s^0} \to \mathrm{D_s^-}\,\mathrm{a_1^+}\,(\phi\,\pi^-)$	10
$\mathrm{B_s^0} \to \mathrm{D_s^-}\,\mathrm{a_1^+}\,(\mathrm{K^{*0}\,K^-})$	5
$\mathrm{B_s^0} \to \mathrm{D_s^-}\,\mathrm{a_1^+}\,(\mathrm{K_S^0\,K^-})$	7

Table 2: Branching ratio values used for the $\mathrm{B_s^0}$ hadronic decay modes.

Decay mode	Branching Ratio (%)
$\mathrm{B_s^0} \to \mathrm{D_s^-}\,\pi^+$	0.28
$\mathrm{B_s^0} \to \mathrm{D_s^{*-}}\,\pi^+$	0.28
$\mathrm{B_s^0} \to \mathrm{D_s^-}\,\mathrm{a_1^+}$	0.76
$\mathrm{B_s^0} \to \mathrm{D_s^{*-}}\,\mathrm{a_1^+}$	0.92
$\mathrm{B_s^0} \to \mathrm{D_s^-}\,\rho^+$	0.76
$\mathrm{B_s^0} \to \mathrm{D_s^{*-}}\,\rho^+$	0.92

within $\pm 70\,\mathrm{MeV}/c^2$ of the nominal $\mathrm{B_s^0}$ mass, $m = (5369.6 \pm 2.4)\,\mathrm{MeV}/c^2$ [1], are selected and are referred to as belonging to the *main peak* region. The event selection efficiencies for the different channels range from 5% to 19%, as shown in Table 1.

4.4 Reconstruction of $\mathrm{B_s^0}$ decays with photons and neutral pions

The procedure described in Sections 4.1–4.3 also selects decays into the $\mathrm{D_s^{*-}}\pi^+$, $\mathrm{D_s^-}\,\rho^+$, $\mathrm{D_s^{*-}}\rho^+$ and $\mathrm{D_s^{*-}a_1^+}$ final states, with a reconstructed invariant mass in the region $5.0 - 5.3\,\mathrm{GeV}/c^2$ (*satellite peak*) due to undetected photons and/or neutral pions. The decay channels considered are implemented in the simulation with the rates given in Table 2.

As an example, the $\mathrm{D_s^-}\,\pi^+$ invariant mass distribution for the $\mathrm{B_s^0} \to \mathrm{D_s^{*-}}\,\pi^+$ decay is shown in Fig. 3. Candidates with $\mathrm{D_s^{*-}} \to \mathrm{D_s^-}\,\gamma$ can be fully reconstructed and used for the oscillation analysis with improved purity if the photon is reconstructed.

The photon coming from the $\mathrm{D_s^{*-}}$ decay is searched for among those reconstructed in the ECAL with the requirement that the mass difference between the reconstructed $\mathrm{D_s^-}\,\gamma$ mass and the nominal $\mathrm{D_s^{*-}}$ mass is within $\pm 100\,\mathrm{MeV}/c^2$. In the case of multiple photon candidates, that giving the smallest mass difference is chosen. The resolution of the invariant mass of the $\mathrm{D_s^{*-}}\,\pi^+$ (or the $\mathrm{D_s^{*-}}\,\mathrm{a_1^+}$) is dominated by the ECAL energy resolution. The energy of the

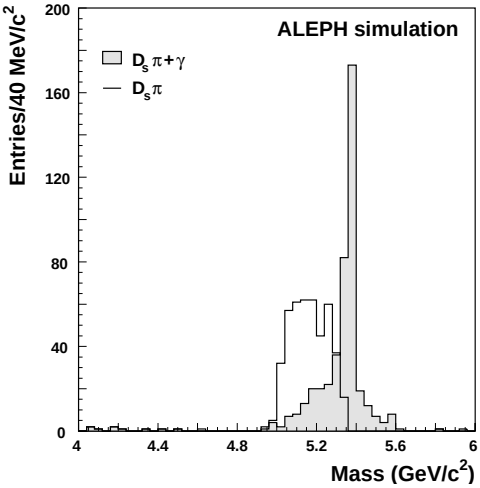

Figure 3: $D_s^- \pi^+$ (empty histogram) and $D_s^- \pi^+ \gamma$ (shaded histogram) invariant mass distribution for simulated events with $B_s^0 \to D_s^{*-} \pi^+$.

selected photon candidate is recomputed with the D_s^{*-} mass constraint, improving the B_s^0 mass resolution from $60\,\mathrm{MeV}/c^2$ to $30\,\mathrm{MeV}/c^2$ (Fig. 3). The simulation indicates that 80% of the selected $D_s^{*-} \to D_s^- \gamma$ decays are fully reconstructed with this method.

For $B_s^0 \to D_s^- \rho^+$ decays a search is performed among all reconstructed π^0's [6] in a cone of 45° around the $D_s^- \pi^+$ direction. The π^0 which forms an invariant mass with the π^+ closest to the ρ^+ mass is selected. Reconstructed B_s^0 candidates must have an invariant mass between $5\,\mathrm{GeV}/c^2$ and $5.4\,\mathrm{GeV}/c^2$. The π^0 momentum is computed rescaling the two photon energies with the π^0 mass constraint. The broad ρ^+ resonance does not allow the π^0 momentum resolution to be further improved. Around 40% of the selected $B_s^0 \to D_s^- \rho^+$ decays in the satellite peak are fully reconstructed with this procedure. For about 25% of the candidates, only one of the photons from the π^0 is found and used.

Finally, the decay mode $B_s^0 \to D_s^{*-} \rho^+$ is reconstructed by applying in turn the two procedures. In some cases the presence of neutral pions and photons compatible with the initial $D_s^- \pi^+$ combination allows multiple B_s^0 decay modes to be successfully reconstructed. If the $D_s^- \pi^+$ invariant mass is below $5.3\,\mathrm{GeV}/c^2$ and the difference between the $D_s^- \pi^+ \gamma$ invariant mass and the nominal B_s^0 mass is larger than $20\,\mathrm{MeV}/c^2$, the combination with both the photon and the π^0 is taken; the $D_s^- \pi^+ \gamma$ combination is taken otherwise.

Candidates which remain in the satellite peak are also used in the analysis but are classified differently to account for different B_s^0 purities and proper-time resolutions.

4.5 Sample composition

The B_s^0 mass spectra of all reconstructed candidates are shown in Fig. 4. Agreement is observed between the data and the prediction from the simulation.

Candidates selected in the main and satellite peaks are used for the oscillation analysis. Twelve classes of events are defined according to the D_s^- decay mode, the number of charged particles accompanying the D_s^- and whether the B_s^0 candidate is reconstructed in the main or

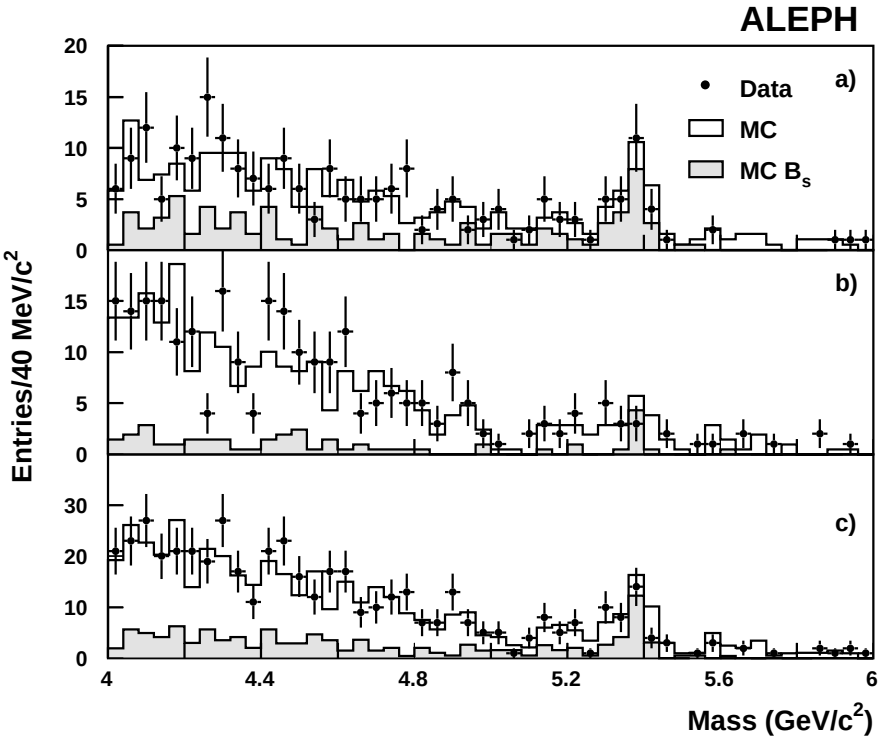

Figure 4: Mass spectra for the reconstructed B_s^0 candidates, in the data (dots with error bars) and the simulation (histograms). The shaded area corresponds to all hadronic B_s^0 decays. The three plots represent a) the $D_s^- \pi^+(\pi^0,\gamma)$ channel; b) the $D_s^- a_1^+(\pi^0,\gamma)$ channel; and c) the sum of the two.

satellite peak. The sample composition is described in terms of signal B_s^0 events, B^0 decays where all decay tracks are selected and at least one particle is misidentified, and B^+ decays with at least one missing and one misidentified particle. The remaining non resonant background consists of about an equal amount of b decays and light quark events, and the b component is further split into mixed and unmixed events. For each background source, the shape and normalization are taken from the simulation. The sample composition and the number of events observed in the data are shown in Table 3, for each class.

For each decay mode, the distributions of the helicity angle and/or the D_s^- invariant mass, different for the signal and the background, are used to estimate the purity of the sample on an event-by-event basis, according to

$$\text{Purity} = \frac{f \cdot \mathrm{P_S}(x)}{f \cdot \mathrm{P_S}(x) + (1-f) \cdot \mathrm{P_B}(x)} \ . \tag{7}$$

Here x is the discriminant variable, f is the average purity, as given in Table 3, and $\mathrm{P_S}$ and $\mathrm{P_B}$ are the aforementioned normalized distributions of x for the signal and background. In the $D_s^- \to \phi\,\pi^-$ decay mode, the helicity angle distribution is used; for the $D_s^- \to K_S^0\,K^-$ decay mode, the D_s^- invariant mass is used; and for the $D_s^- \to K^{*0}\,K^-$ decay mode, the product of the two probability density functions is used instead.

Table 3: Expected fractions (in %) of signal and background events in the two mass regions and for different decay channels, and number of observed events in the data.

Class		Composition (%)				Data
Region	Channel	B_s^0	B^0	B^+	Non resonant	Candidates
Main peak	$\phi\,\pi^-$	81 ± 7	4	2	13	4
$D_s^-\,\pi^+(\pi^0,\gamma)$	$K^{*0}\,K^-$	50 ± 8	12	3	35	12
	$K_S^0\,K^-$	29 ± 8	47	0	24	5
Satellite peak	$\phi\,\pi^-$	82 ± 9	6	6	6	7
$D_s^-\,\pi^+(\pi^0,\gamma)$	$K^{*0}\,K^-$	32 ± 7	23	8	37	7
	$K_S^0\,K^-$	37 ± 7	21	0	42	9
Main peak	$\phi\,\pi^-$	38 ± 7	4	0	58	6
$D_s^-\,a_1^+(\pi^0,\gamma)$	$K^{*0}\,K^-$	29 ± 7	5	0	66	3
	$K_S^0\,K^-$	20 ± 7	16	0	64	2
Satellite peak	$\phi\,\pi^-$	21 ± 7	9	0	70	6
$D_s^-\,a_1^+(\pi^0,\gamma)$	$K^{*0}\,K^-$	12 ± 4	9	0	79	9
	$K_S^0\,K^-$	7 ± 4	9	0	84	10

In the $D_s^-\,a_1^+$ channel, because of the a_1^+ width, the combinatorial background comes mostly from b-hadron decays in which some of the pions make coincidentally a B_s^0 mass in the selected region. In the $D_s^-\pi^+$ channel, the main source of non-B_s^0 decays are D^- reflections from $B^0 \to D^-\,\pi^+$. The simulation predicts that this source affects mainly the $K^{*0}\,K^-$ channel, because the K^{*0} resonance is broader than the ϕ and a $D^- \to K^{*0}\,\pi^-$ decay can fake a $D_s^- \to K^{*0}\,K^-$ decay if the π^- is misidentified as a K^-. Out of 1300 generated B^0 decays, eleven remain in the mass peak (within $\pm 70\,\mathrm{MeV}/c^2$ of the B_s^0 mass). With the branching ratios $\mathrm{BR}(B^0 \to D^-\pi^+) = (3.0 \pm 0.4) \times 10^{-3}$ and $\mathrm{BR}(D^- \to K^-\pi^-\pi^+) = (9.0 \pm 0.6)\%$ [1], (1.5 ± 0.2) B^0 decays are expected to be present in the $B_s^0 \to D_s^-\,\pi^+$, $D_s^- \to K^{*0}\,K^-$ channel.

A total of 44 events is observed in the $D_s^-\,\pi^+(\pi^0,\gamma)$ channel, of which 10.7 and 11.3 are expected to come from a B_s^0 decay in the main and satellite peak, respectively. In the $D_s^-\,a_1^+(\pi^0,\gamma)$ channel, 36 events are reconstructed, of which 3.6 and 3.0 are expected from signal in the two mass regions.

4.6 Proper-time measurement

The decay length is calculated as the distance between the B_s^0 vertex and the primary vertex projected onto the direction of the B_s^0 momentum. The average B_s^0 decay length resolution is estimated from simulated events to be about $180\,\mu$m. The pull of the decay length distribution for fully reconstructed candidates is fitted with the sum of two Gaussian functions of widths $\sigma_1 = 1.03 \pm 0.03$ and $\sigma_2 = 2.1 \pm 0.8$, the latter accounting for only 5% of the total. For candidates in the satellite peak, the width is consistent with a single Gaussian function of width

$\sigma = 1.08 \pm 0.06$. In the oscillation fit, the decay length uncertainty is evaluated on an event-by-event basis, and corrected for these pulls.

The boost of the B_s^0 is calculated as the ratio between its measured energy and its reconstructed invariant mass. The relative boost resolution is described by the sum of two Gaussian functions. For candidates in the main peak, the resolution is of the order of 0.5% yielding a proper-time resolution of about 0.08 ps. Candidates in the satellite peak have still a good boost resolution, of about 3%, because the effect of the missing photon or π^0 largely cancels in the ratio of reconstructed energy and mass.

4.7 Control sample

Fully reconstructed B^+ mesons are used to check the accuracy of the simulation. Such a sample profits from a production rate larger than that of B_s^0 mesons and from a better knowledge of the different decay modes. In addition, the initial-state flavour is unambiguously determined by the total electric charge, allowing the performance of the initial-state tag to be tested.

The B^+ meson candidates are selected in the $B^+ \to D^0\pi^+$ decay mode, with the D^0 reconstructed in the final states $D^0 \to K^-\pi^+$, $D^0 \to K^-\pi^+\pi^0$, and $D^0 \to K^-\pi^+\pi^-\pi^+$. The reconstructed B^+ must satisfy the kinematical cuts used for the B_s^0 reconstruction, as described in Section 4.3. The resulting invariant mass distribution is shown in Fig. 5a with a clear peak

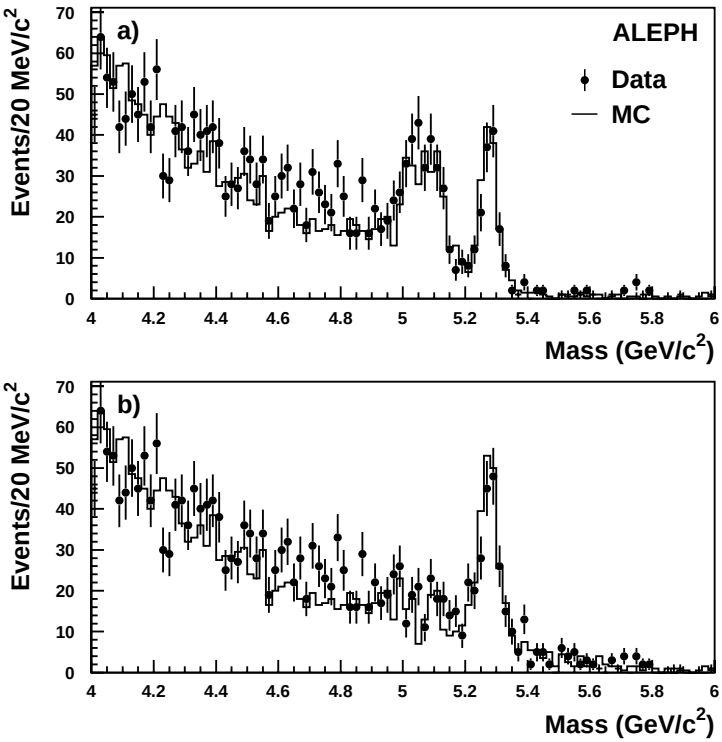

Figure 5: Invariant mass distribution for the B^+ selected sample, a) before and b) after applying the photon and π^0 recovery algorithm, in the data (dots with error bars) and the simulation (histogram).

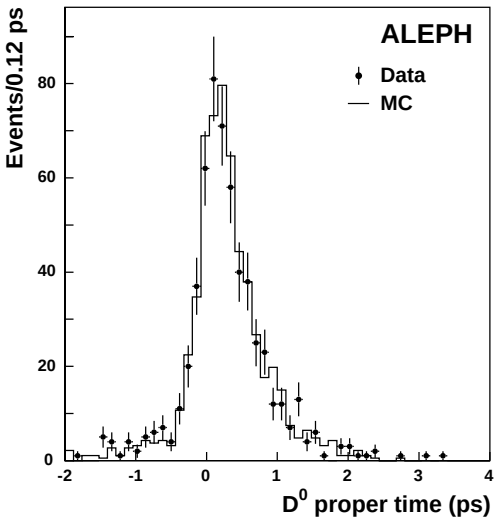

Figure 6: Reconstructed proper time of the D^0 candidates, for the data (dots with error bars) and the simulation (histogram). In this figure, the cut on the distance between the D^0 and the B^+ is not applied.

at the B^+ mass, and a satellite peak due to $B^+ \to D^{*0}\pi^+$ decays in which the π^0 from the $D^{*0} \to D^0\pi^0$ decay is not reconstructed. Some of these decays can be fully reconstructed by looking for a π^0 in a cone around the B meson direction, as described in Section 4.4. The corrected mass distribution is displayed in Fig. 5b.

Altogether 271 B^+ candidates are reconstructed with an estimated purity of about 94%. The invariant mass distribution, the efficiency of the π^0 reconstruction and the D^0 proper time (Fig. 6) are well predicted by the simulation.

The B^+ candidates are used to check the initial-state mistag probability in the data. Due to isospin conjugation, the charge related variables in the hemisphere containing the B^+ meson used in the initial-state tag neural network have to be reversed to be effective in the discrimination. The effective initial-state mistag probability of the B^+ sample is measured to be $(22.4 \pm 4.2)\%$, in good agreement with the prediction of the simulation, $(22.5 \pm 2.8)\%$.

The opposite-side tag alone can also be tested. An effective value of $(25.0 \pm 5.1)\%$ is found in the data and $(25.9 \pm 3.7)\%$ in the simulation, in agreement with the measurement made in Ref. [13].

4.8 The B_s^0 oscillations results

The likelihood functions of the B_s^0 signal, the B^0 and the B^+ backgrounds are built as explained in Section 3.4. The functions which describe the proper-time distribution of the three B-meson species in Eq. 4 are folded with a resolution function and with the reconstruction efficiencies. The selection cut on the decay length significance significantly reduces the efficiency at small proper times. The proper time distributions of the other three background components are extracted from the simulation.

The amplitude spectrum, the result of the likelihood fit to the sample of fully reconstructed B_s^0 candidates, is shown in Fig. 7. A 95% C.L. lower limit on the B_s^0 oscillation frequency is

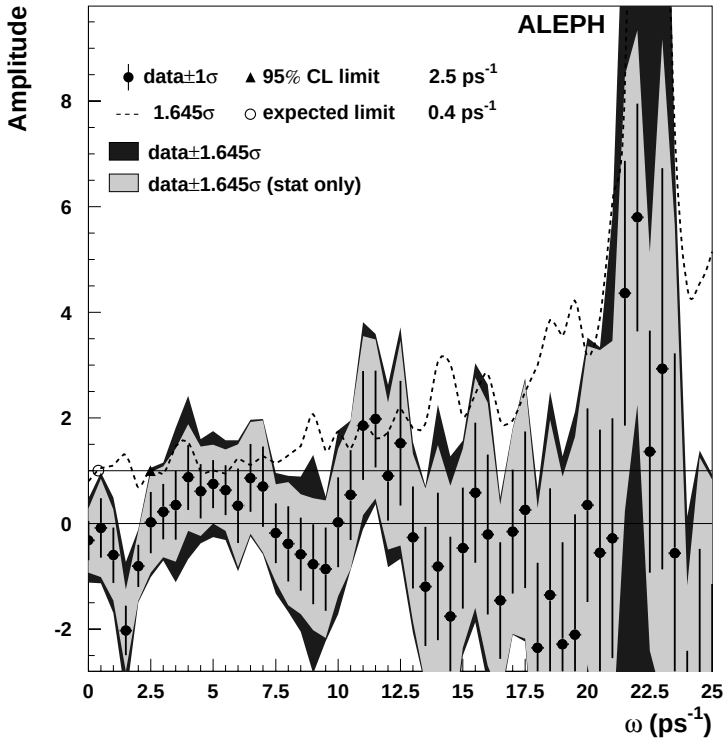

Figure 7: Fitted oscillation amplitude as a function of the test frequency in the sample of fully reconstructed B_s^0 candidates.

set with this sample alone at $\Delta m_s > 2.5\,\mathrm{ps}^{-1}$, with an expected limit of $0.4\,\mathrm{ps}^{-1}$. The most important feature is the relatively small amplitude uncertainty at high values of the oscillation frequency.

4.8.1 Systematic Uncertainties

Uncertainties in the evaluation of the fit input parameters are accounted for as explained in Section 3.4. All systematic effects studied are summarized in Table 4.

The purity is determined according to Eq. 7 with the predictions quoted in Table 3. The systematic uncertainty on the background parametrization has been assessed by varying both the shapes and the fractions of the different components. In particular, the B^+ and B^0 fractions have been varied by 50%. For the non resonant background, the ratio between the light quark and b fractions has been varied by 40%, the ratio between the mixed and unmixed b events has been varied by 10%; the uncertainty in their shapes has been estimated by changing the B^0 content by a factor of two. These variations account for the limited statistics of the simulated background sample.

It is expected, from factorization and SU(3) symmetry, that the B_s^0 branching ratios equal those of the corresponding equivalent B^0 decays. The uncertainty of these predictions is taken to be 30% for each of the branching ratios.

The effect of the uncertainties in the parametrization of the momentum resolution is

Table 4: Systematic uncertainties on the fitted amplitude at different test oscillation frequency values compared to the statistical uncertainty, for the selection of hadronic B_s^0 decays. The shift of both the measured amplitude, $\Delta\mathcal{A}$, and of its statistical uncertainty, $\Delta\sigma$, are listed for each parameter, signed according to their change when the parameter is increased.

Oscillation frequency		0 ps^{-1}	10 ps^{-1}	15 ps^{-1}	20 ps^{-1}	25 ps^{-1}
Statistical uncertainty		0.371	0.848	1.146	1.831	3.068
Branching Ratio	$\Delta\mathcal{A}$	+0.142	−0.355	+0.181	−0.215	+0.007
	$\Delta\sigma$	+0.012	+0.074	+0.021	+0.095	negl.
B_s^0 Purity	$\Delta\mathcal{A}$	+0.232	−0.617	+0.318	−0.336	−0.197
	$\Delta\sigma$	+0.029	+0.158	+0.066	+0.218	negl.
Momentum Resolution	$\Delta\mathcal{A}$	+0.004	−0.014	+0.065	−0.009	+0.222
	$\Delta\sigma$	+0.003	+0.005	+0.007	+0.015	negl.
Decay length resolution	$\Delta\mathcal{A}$	negl.	+0.005	−0.043	+0.006	−0.356
	$\Delta\sigma$	negl.	+0.009	+0.027	+0.062	negl.
Mistag	$\Delta\mathcal{A}$	+0.151	+0.008	+0.193	+0.286	+0.191
	$\Delta\sigma$	negl.	+0.035	+0.021	+0.106	negl.
Decay length scale	$\Delta\mathcal{A}$	negl.	+0.088	−0.185	−0.075	−0.330
	$\Delta\sigma$	negl.	+0.005	+0.070	+0.140	+0.661
$\tau_{B_s^0}$	$\Delta\mathcal{A}$	−0.005	+0.013	−0.013	+0.027	−0.024
	$\Delta\sigma$	−0.001	negl.	−0.002	−0.007	+0.031
$\Delta\Gamma_s$	$\Delta\mathcal{A}$	+0.080	+0.113	+0.082	+0.324	+0.065
	$\Delta\sigma$	negl.	negl.	negl.	negl.	negl.
B^+ proportion	$\Delta\mathcal{A}$	−0.007	+0.005	−0.015	+0.003	+0.021
	$\Delta\sigma$	+0.002	+0.003	+0.008	+0.007	+0.008
B^0 proportion	$\Delta\mathcal{A}$	−0.005	−0.019	−0.006	−0.071	+0.052
	$\Delta\sigma$	+0.008	+0.012	+0.012	+0.029	−0.042
udsc proportion	$\Delta\mathcal{A}$	−0.003	+0.017	+0.011	−0.060	+0.115
	$\Delta\sigma$	−0.001	−0.011	−0.005	+0.016	−0.088
mixed fraction of B back	$\Delta\mathcal{A}$	−0.021	−0.001	−0.013	−0.013	+0.017
	$\Delta\sigma$	−0.001	−0.003	−0.002	−0.007	−0.019
B background shape	$\Delta\mathcal{A}$	+0.004	negl.	+0.005	+0.018	+0.004
	$\Delta\sigma$	negl.	+0.001	negl.	negl.	+0.010
Total systematic uncertainty		0.312	0.632	0.464	0.605	0.606

evaluated by varying each parameter by the corresponding uncertainty (Section 4.6).

The B^+ candidates reconstructed with a negative D^0 decay length (Section 4.7) are used to check the B_s^0 decay length resolution. A discrepancy of about 3% is found between data and simulation and taken as the corresponding systematic uncertainty.

The fully reconstructed B^+ mesons are used to measure the initial-state mistag probability. Agreement within statistics is observed between data and simulation. The systematic uncertainty is evaluated by varying the slope and the offset of the mistag calibration by the statistical accuracy of the comparison (about 20% relative), with the method of Ref. [13].

The statistical accuracy resulting from the fit to the B_s^0 proper time (Section 4.8.2) is used to assess the systematic uncertainty from any discrepancy between data and simulation on the decay length scale.

The uncertainties on the world average B_s^0 lifetime and B^0 oscillation frequency [1] are

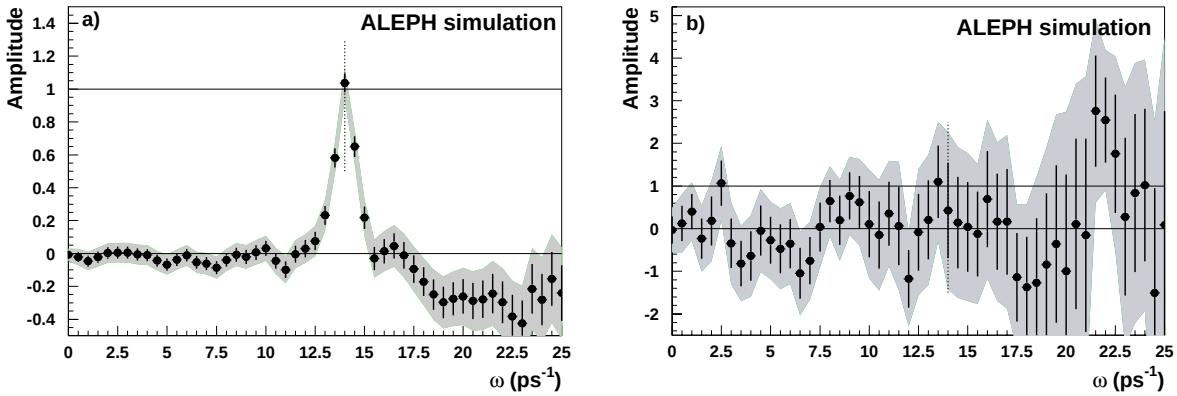

Figure 8: Amplitude spectrum for a) a large sample of simulated signal events in the $\mathrm{D_s^-}\,\pi^+$ decay channel, and b) exclusively reconstructed $\mathrm{B_s^0}$ candidates selected in an unbiased $\mathrm{Z} \to \mathrm{q\overline{q}}$ sample corresponding to about twice the data statistics. The shaded area represents $\pm 1.645\,\sigma_{\mathcal{A}}^{\mathrm{stat}}$. In both cases the value of Δm_{s} chosen in the simulation, $\omega = \Delta m_{\mathrm{s}}^{\mathrm{MC}}$, is indicated with a dotted line.

propagated to the amplitude scan. The effect of Δm_{d} is found to be negligible and is not included in Table 4.

Finally, the amplitude scan is repeated with a likelihood function taking into account the width difference $\Delta\Gamma_{\mathrm{s}}/\Gamma_{\mathrm{s}} = 0.16^{+0.08}_{-0.09}$ [18] between the two $\mathrm{B_s^0}$ mass eigenstates and the difference is taken as a systematic uncertainty.

4.8.2 Checks

The oscillation fit performed with a simulated sample of $\mathrm{B_s^0} \to \mathrm{D_s^-}\,\pi^+$ decays leads to an amplitude compatible with zero at low frequency values and compatible with unity at $\Delta m_{\mathrm{s}} = 14\,\mathrm{ps}^{-1}$, as shown in Fig. 8a. The oscillation frequency fitted from this sample is $\Delta m_{\mathrm{s}} = 14.03 \pm 0.03\,\mathrm{ps}^{-1}$.

The amplitude scan done with an unbiased $\mathrm{Z} \to \mathrm{q\overline{q}}$ simulated sample shows that the exclusive $\mathrm{B_s^0}$ search is not sensitive enough to clearly resolve the signal (Fig. 8b); nevertheless the fitted amplitude is compatible with zero at low frequency values and with unity at $\omega = \Delta m_{\mathrm{s}}^{\mathrm{MC}}$.

Finally, a fit to the $\mathrm{B_s^0}$ lifetime performed on the data leads to $\tau_{\mathrm{B_s^0}} = (1.58 \pm 0.11)\,\mathrm{ps}$ (statistical uncertainty only), in agreement with the the present world average [1].

5 Analysis of $\mathrm{D_s^-}\,\ell^+$ pairs

The second analysis is based on the reconstruction of semileptonic $\mathrm{B_s^0}$ decays

$$\mathrm{B_s^0} \to \mathrm{D_s^{(*)-}}\,\ell^+\,\nu_\ell\ ,$$

where the $\mathrm{D_s^-}$ decays into one of the following hadronic and semileptonic decay modes

$$\begin{array}{ll}
\mathrm{D_s^-} \to \phi\,\pi^-\,, & \mathrm{D_s^-} \to \mathrm{K^{*0}\,K^-}\,, \\
\mathrm{D_s^-} \to \mathrm{K_S^0\,K^-}\,, & \mathrm{D_s^-} \to \phi\,\rho^-\,, \\
\mathrm{D_s^-} \to \mathrm{K^{*0}\,K^{*-}}\,, & \mathrm{D_s^-} \to \phi\,\pi^+\,\pi^-\,\pi^-\,, \\
\mathrm{D_s^-} \to \phi\,\mathrm{e^-}\,\bar{\nu}_{\mathrm{e}}\,, & \mathrm{D_s^-} \to \phi\,\mu^-\,\bar{\nu}_\mu\ .
\end{array}$$

Table 5: Momentum cuts (in GeV/c) applied for the different decay modes.

$\phi\,\pi^-$	$\mathrm{K}^{*0}\,\mathrm{K}^-$	$\mathrm{K}^0_\mathrm{S}\,\mathrm{K}^-$	$\phi\,\rho^-$	$\mathrm{K}^{*0}\,\mathrm{K}^{*-}$	$\phi\,\pi^+\,\pi^-\,\pi^-$	$\phi\,\mathrm{e}^-\,\bar{\nu}_\mathrm{e}$	$\phi\mu^-\bar{\nu}_\mu$
$p_\pi > 1$ $p_\phi > 3$	$p_\pi > 1$ $p_\mathrm{K} > 2$ $p_{\mathrm{K}^{*0}} > 3.5$	$p_\mathrm{K} > 2$	$p_\pi > 1$	$p_{\mathrm{K}^+} > 3$ $p_{\mathrm{K}^{*0}} > 4$ $p_{\mathrm{K}^{*-}} > 3$	$p_\phi > 3$	$p_\phi > 4$	$p_\phi > 3.5$

The unstable decay products of the D_s^- are reconstructed as $\phi \to \mathrm{K}^+\,\mathrm{K}^-$, $\mathrm{K}^{*0} \to \mathrm{K}^+\,\pi^-$, $\mathrm{K}^{*-} \to \mathrm{K}^0_\mathrm{S}\,\pi^-$, $\mathrm{K}^0_\mathrm{S} \to \pi^+\,\pi^-$, and $\rho^- \to \pi^-\,\pi^0$.

5.1 Event selection

The event selection is reoptimized with respect to Ref. [3], in order to exploit the improved $\mathrm{d}E/\mathrm{d}x$ estimate and the better tracking resolution resulting from the data reprocessing.

The charged kaon and pion candidates are selected by requiring that their momenta satisfy $p_\mathrm{K} > 1\,\mathrm{GeV}/c$ and $p_\pi > 0.5\,\mathrm{GeV}/c$ and that $\chi_\mathrm{K} + \chi_\pi < 0$ and $|\chi_\pi| < 3$, respectively. Electron and muon candidates (called "leptons" hereafter) are selected as described in Ref. [19]. Neutral kaons and neutral pions are reconstructed as described in Ref. [6]. Their momenta must satisfy $p_{\mathrm{K}^0_\mathrm{S}} > 2\,\mathrm{GeV}/c$ and $p_{\pi^0} > 1\,\mathrm{GeV}/c$, respectively.

Other selection cuts are applied in each channel to decay particle and resonance momenta, the reconstructed D_s^- momentum, and the reconstructed B_s^0 momentum, as summarized in Table 5. The invariant masses of the resonances must lie within $\pm 9\,\mathrm{MeV}/c^2$ and $\pm 50\,\mathrm{MeV}/c^2$ of the nominal ϕ and K^{*0} mass, respectively. In the $\phi\,\pi^-$ and $\mathrm{K}^{*0}\,\mathrm{K}^-$ channels, the helicity angle λ must satisfy $|\cos\lambda| > 0.4$. In addition, for the $\mathrm{K}^{*0}\,\mathrm{K}^-$ mode, it is required that $|\cos\beta| < 0.8$, where β is the angle between the K^{*0} and the D_s^- flight direction estimated in the centre-of-mass system of the D_s^-: the distribution is expected to be flat for the signal because the D_s^- has spin zero, and peaked at 1 for the background. The mass of the reconstructed D_s^- candidate is required to be compatible with its nominal value [1]. The size of the mass windows of the selected candidates depends on the reconstructed channel. It varies between $\pm 10\,\mathrm{MeV}/c^2$ and $\pm 60\,\mathrm{MeV}/c^2$ for the hadronic D_s^- reconstruction and is $\pm 6\,\mathrm{MeV}/c^2$ for the ϕ in the semileptonic channels.

The $\mathrm{D}_\mathrm{s}^-\,\ell^+$ invariant mass is required to lie between 3 (2.5) GeV/c^2 and $5.5\,\mathrm{GeV}/c^2$ in all hadronic (semileptonic) D_s^- decay channels.

For all the decay channels except $\mathrm{K}^0_\mathrm{S}\,\mathrm{K}^-$, at least two charged decay products must be reconstructed with at least one VDET hit in both $r\phi$ and z projections (only one for the $\mathrm{K}^0_\mathrm{S}\,\mathrm{K}^-$ mode). The D_s^- decay particles must form a vertex with a fit probability of at least 1%.

The lepton and D_s^- candidates in each hemisphere are required to form a common vertex with a fit probability larger than 1%. If more than one pair in the same decay mode can be formed, only that with the leading lepton is selected. If several pairs share the leading lepton candidate, that with the most energetic D_s^- is kept.

The uncertainty on the distance from the primary vertex to the B_s^0 (D_s^-) decay vertex must be less than $500\,\mu\mathrm{m}$ (1 mm) and the significance of the distance between the B_s^0 and the D_s^-

Table 6: Selection efficiency (with an uncertainty of 0.1% absolute), size and composition of the selected samples for the $D_s^- \ell^+$ analysis. The selection efficiencies and background compositions are obtained from the simulation while the signal purities are extracted from the data (Section 5.3).

Channel	Efficiency (%)	Candidates	Signal	$b \to D_s^\pm D X$	D^- Refl.	Comb. backg.		
						uds	$c\overline{c}$	$b\overline{b}$
$\phi\,\pi^-$	13.1	82	54.0	15.7	0	3.4	3.1	5.8
$K^{*0}\,K^-$	8.5	120	46.0	19.5	18	3.1	5.7	27.6
$K_S^0\,K^-$	2.3	17	5.8	2.0	0.4	0.7	2.4	5.7
$\phi\,\rho^-$	2.4	40	11.2	2.4	0.6	1.1	1.1	23.5
$K^{*0}\,K^{*-}$	3.4	21	9.4	2.6	0	0.6	1.2	7.2
$\phi\,\pi^+\,\pi^-\,\pi^-$	6.8	17	8.4	1.8	0	0.2	0.2	6.3
$\phi\,e^-\,\bar{\nu}_e$	6.6	17	9.3	2.4	0	0.3	0.0	5.0
$\phi\,\mu^-\,\bar{\nu}_e$	4.6	19	11.4	1.2	0	0.0	0.0	6.4

decay vertices projected along the D_s^- momentum must be larger than -0.5. These cuts reduce significantly the $b \to D_s^\pm D X$ background because, in this case, the lepton and the D_s^- come from different vertices.

The selection efficiencies, the numbers of selected candidate events and the estimated composition of the data sample are listed in Table 6.

5.2 Proper-time reconstruction

The decay proper time of each B_s^0 candidate is obtained from Eq. 2, with the nominal B_s^0 mass [1]. The decay length is estimated as the distance between the primary vertex and the $D_s^- \ell^+$ vertex projected onto the $D_s^- \ell^+$ momentum. This procedure introduces a small negative bias of the order of $-20\,\mu$m for the signal. The B_s^0 momentum is computed from the reconstructed momentum of the D_s^-, the lepton momentum, and the neutrino energy E_ν. The latter is estimated from the missing energy in the hemisphere, corrected with the hemisphere masses as in Ref. [20].

The resolution function for the B_s^0 decay length is represented by the sum of two Gaussian functions with common mean. The parameters are estimated with simulated events, separately for each decay channel. The pull distributions show that the decay length uncertainty is consistently underestimated by about 10%. This effect is due to the projection onto the $D_s^- \ell^+$ momentum direction which only approximates the B_s^0 flight direction. Once the pull correction is applied, the B_s^0 decay length uncertainty for the signal is, on average, about $240\,\mu$m. An independent parametrization is performed for the background from cascade decays, both for the bias and the decay length resolution.

Similarly, the distribution of $(p - p_0)/p_0$, where p and p_0 are the reconstructed and true B_s^0 momenta, is fitted with the sum of two Gaussian functions in bins of the reconstructed B_s^0 momentum. The average relative uncertainty on the momentum is predicted to be about 11%.

The proper-time distribution for the combinatorial background is taken from the simulation. It agrees with the distribution built with data from the side bands of the mass distribution.

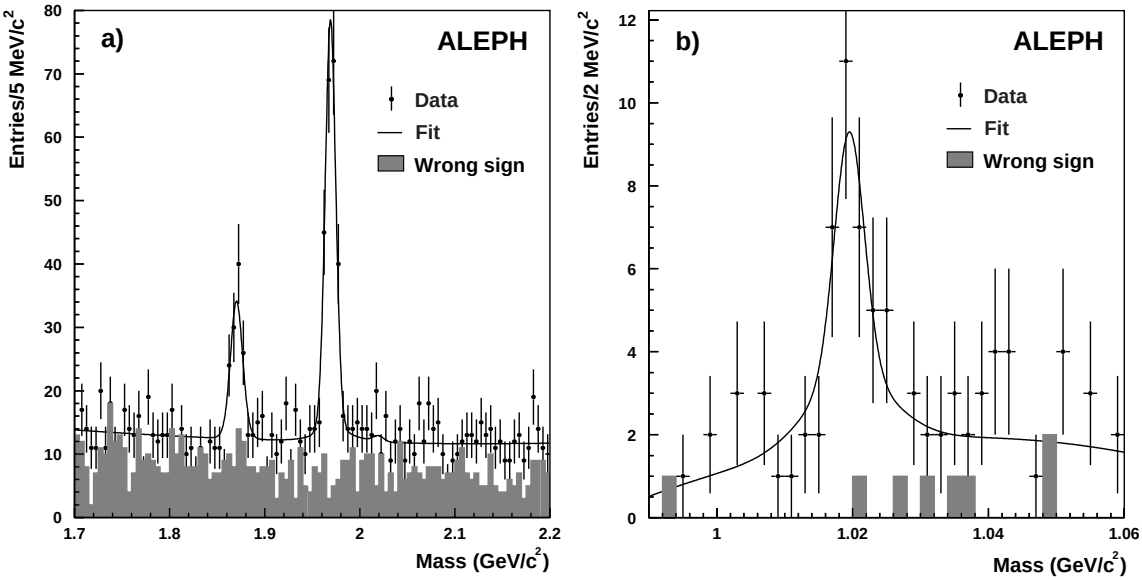

Figure 9: Mass distribution of a) the selected D_s^- candidates with $D_s^- \ell^+$ combinations for hadronic D_s^- decays, and b) the selected ϕ candidates for semileptonic D_s^- decays in the data (dots with error bars). The fit result is superimposed. The shaded histogram shows the spectrum for the wrong sign combinations.

5.3 Sample composition

The mass spectra of the reconstructed D_s^- (ϕ) in the hadronic (semileptonic) candidates show a clear peak around the expected mass (Fig. 9). The peak at lower mass comes from $D^+ \to K^+ K^- \pi^+$ decays. The spectrum is fitted with the sum of two Gaussian functions for the signal peak and a second degree polynomial for the combinatorial background for each channel considered. For the $\phi \pi^+ \pi^- \pi^-$ channel, an additional peak is allowed for in the fit at higher mass to account for the decay $D^{*+} \to D^0 \pi^+$, $D^0 \to \phi \pi^+ \pi^-$. The relative normalization of the functions is fitted on the data for each channel, while their shapes are determined from the simulation.

The processes which contribute to the resonant component of the sample are the $B_s^0 \to D_s^- \ell^+ \nu$ signal, B_s^0 hadronic decays with a misidentified lepton, $b \to D_s^\pm D X$ ($D \to \ell$) decays, and reflections from $b \to D^- \ell \nu X$ decays, where a pion from the D^- is identified as a kaon. The total fraction of "resonant" candidates, in a mass window around the nominal D_s^- (or ϕ) mass, is expressed with Eq. 7 on an event-by-event basis as a function of the reconstructed D_s^- (or ϕ) mass, with the reconstructed mass as discriminant variable.

The discrimination between the $D_s^- \ell^+$ signal and cascade decays is performed by a neural network. Compared to the previously published analysis [3], this procedure provides a better discrimination power. The inputs to the network are the momentum and the transverse momentum with respect to the jet closest to the lepton, the $D_s^- \ell^+$ invariant mass, the B_s^0 momentum, and the number of charged particles which form a vertex with the lepton. The distribution of the neural network output for simulated signal and background events is shown in Fig. 10. A slight discrepancy is observed between data and simulation in the output of the network, although with low statistical significance. The effect of this discrepancy is taken

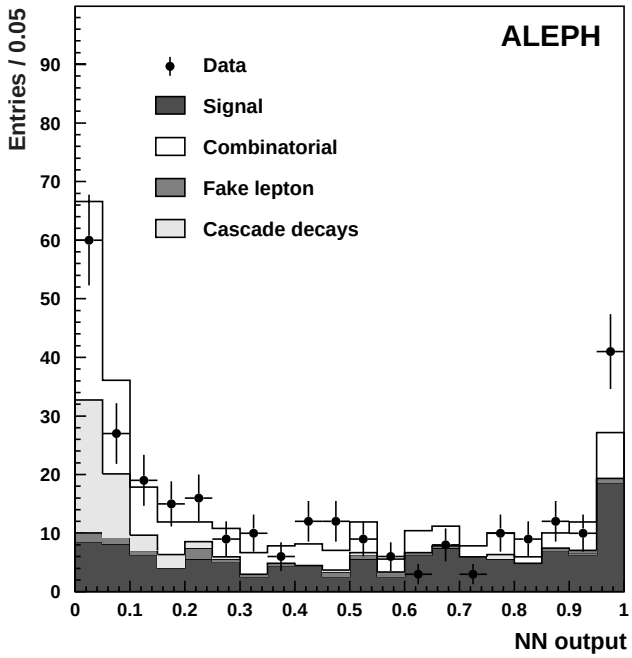

Figure 10: Neural network output for the discrimination of cascade $b \to D_s^{\pm} D X$ decays, for the data (dots with error bars) and the simulation (histograms).

into account in the systematic uncertainties by variation of the signal-to-background ratio (Section 5.4.1).

5.4 The B_s^0 oscillations results

The likelihood functions of the B_s^0 signal and $b \to D_s^{\pm} D X$ cascade decays are built from the analytical proper-time probability density functions, as explained in Section 3.4. The signal selection does not introduce a distortion in the proper-time distribution, and therefore no correction is applied. The proper-time distributions for the combinatorial background are extracted from the simulation; different functions are used for mixed and unmixed B^0 candidates. The result of the fit of the oscillating term amplitude as a function of the test oscillation frequency is shown in Fig. 11. All frequency values below $7.2\,\mathrm{ps}^{-1}$ are excluded at 95% C.L., in agreement with the expected limit of the analysis ($7.5\,\mathrm{ps}^{-1}$).

5.4.1 Systematic uncertainties

Uncertainties in the evaluation of the fit input parameters are accounted for as explained in Section 3.4. The fraction of resonant B_s^0 decays fitted from data is varied by its uncertainty for each decay mode separately. The ratio between the production rates of $B_s^0 \to D_s^{(*)-} \ell^+ \nu$ decays and cascade decays is evaluated to be 1.10 ± 0.21 [1] and is varied by its uncertainty to derive the corresponding systematic uncertainty.

The uncertainty on the initial-flavour mistag rate determination is evaluated as in

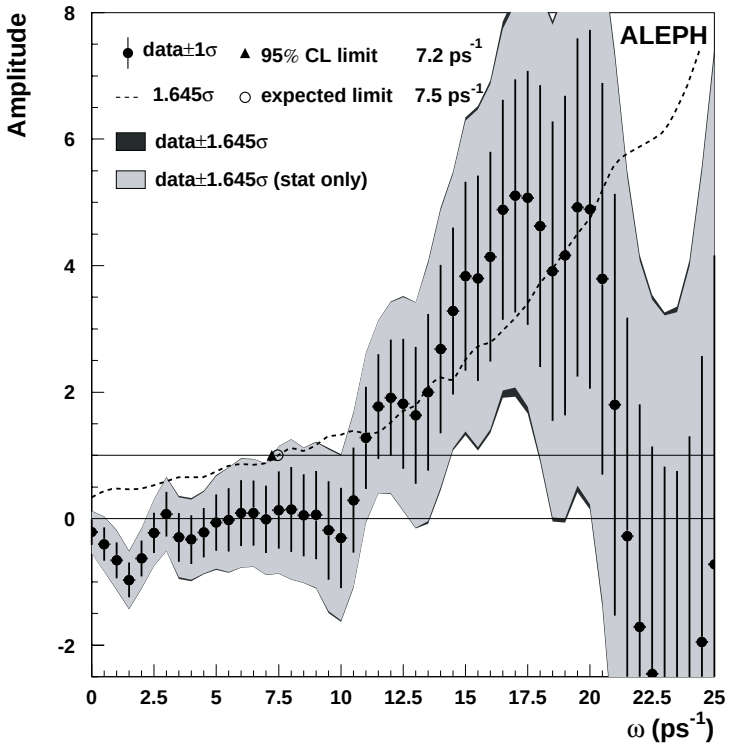

Figure 11: Fitted amplitude spectrum as a function of the test frequency ω for the $\mathrm{D_s^-}\,\ell^+$ sample.

Section 4.8.1, as the same flavour-tag neural network is used in both cases. The impact of a variation of $20\,\mathrm{MeV}/c$ in the reconstructed $\mathrm{B_s^0}$ momentum and of 1% in its uncertainty are assessed. These figures are consistent with the uncertainties estimated in Ref. [20]. The decay length and its uncertainty are also varied, by half of the estimated decay length bias and by 3% respectively (Section 4.8.1). The amplitude scan is redone with a likelihood function taking into account a nonzero value of $\Delta\Gamma_\mathrm{s}$ as described in Section 3.

The contributions of all the systematic sources to the amplitude uncertainty are summarized in Table 7.

5.4.2 Checks

Simulated events are used to check the fitting procedure and signal description. A first check is made with $\mathrm{B_s^0} \to \mathrm{D_s^-}\,\ell^+$ signal events. A likelihood fit for Δm_s leads to $\Delta m_\mathrm{s} = (13.5 \pm 0.6)\,\mathrm{ps}^{-1}$, in agreement with the input value of $14\,\mathrm{ps}^{-1}$. The corresponding amplitude scan is shown in Fig. 12a: the fitted amplitude is compatible with zero below the true oscillation frequency and compatible with unity at $\omega = \Delta m_\mathrm{s}^\mathrm{MC}$. Selected candidates in simulated unbiased $\mathrm{Z} \to \mathrm{q\overline{q}}$ decays are used to check the overall description of the data sample. The result of the amplitude fit, displayed in Fig. 12b, shows that the $\mathrm{D_s^-}\,\ell^+$ selection is not sensitive enough to clearly resolve the signal; nevertheless the fitted amplitude is compatible with zero at low frequency and with unity at $\omega = \Delta m_\mathrm{s}^\mathrm{MC}$.

The $\mathrm{B_s^0}$ lifetime is measured on a simulated sample as $\tau_{\mathrm{B_s^0}} = (1.45 \pm 0.06)\,\mathrm{ps}$, consistent with

Table 7: Systematic uncertainties on the amplitude in the $D_s^- \ell^+$ analysis at different values of the test oscillation frequency. For comparison, the statistical uncertainty is also given.The shift of both the measured amplitude, $\Delta\mathcal{A}$, and of its statistical uncertainty, $\Delta\sigma$, are listed for each parameter, signed according to their change when the parameter is increased.

Oscillation frequency		0 ps^{-1}	10 ps^{-1}	15 ps^{-1}	20 ps^{-1}	25 ps^{-1}
Statistical uncertainty		0.202	0.791	1.494	2.835	4.886
Resonant fraction in $\phi\pi^-$	$\Delta\mathcal{A}$	+0.001	+0.006	−0.059	−0.065	+0.200
	$\Delta\sigma$	−0.001	−0.007	−0.018	−0.041	−0.105
Resonant fraction in $K^{*0}K^-$	$\Delta\mathcal{A}$	+0.001	+0.007	−0.022	+0.016	+0.041
	$\Delta\sigma$	−0.001	−0.003	−0.003	−0.009	−0.031
Resonant fraction in $K_S^0K^-$	$\Delta\mathcal{A}$	+0.001	+0.042	+0.009	−0.237	−0.338
	$\Delta\sigma$	−0.001	−0.005	−0.005	−0.011	−0.096
Resonant fraction in $\phi\rho^-$	$\Delta\mathcal{A}$	+0.002	+0.028	+0.082	−0.130	−0.036
	$\Delta\sigma$	−0.002	−0.011	−0.019	−0.025	−0.022
Resonant fraction in $K^{*0}K^{*-}$	$\Delta\mathcal{A}$	−0.002	+0.009	−0.082	−0.124	−0.004
	$\Delta\sigma$	−0.001	−0.003	+0.003	−0.002	−0.020
Resonant fraction in $\phi\pi^+\pi^-\pi^-$	$\Delta\mathcal{A}$	+0.007	−0.016	−0.145	−0.066	−0.045
	$\Delta\sigma$	−0.001	−0.005	−0.034	−0.015	−0.009
Resonant fraction in $\phi e^-\bar{\nu}$	$\Delta\mathcal{A}$	+0.007	+0.025	+0.040	+0.045	+0.159
	$\Delta\sigma$	−0.001	−0.001	−0.008	−0.010	−0.004
Resonant fraction in $\phi\mu^-\bar{\nu}$	$\Delta\mathcal{A}$	+0.008	−0.013	+0.010	+0.006	negl.
	$\Delta\sigma$	−0.002	−0.002	−0.002	−0.001	negl.
Signal-to-background ratio	$\Delta\mathcal{A}$	+0.017	−0.002	−0.126	−0.183	−0.018
	$\Delta\sigma$	−0.007	−0.017	−0.034	−0.062	−0.093
Neural network purity	$\Delta\mathcal{A}$	+0.003	+0.012	−0.041	−0.045	−0.185
	$\Delta\sigma$	−0.001	−0.004	+0.001	−0.005	+0.013
Mistag	$\Delta\mathcal{A}$	+0.020	+0.119	+0.020	+0.101	+0.598
	$\Delta\sigma$	+0.002	+0.005	+0.058	+0.088	+0.044
Momentum bias	$\Delta\mathcal{A}$	negl.	−0.002	−0.008	+0.012	−0.035
	$\Delta\sigma$	negl.	negl.	−0.005	−0.005	−0.010
Momentum resolution	$\Delta\mathcal{A}$	negl.	+0.013	+0.012	−0.114	+0.291
	$\Delta\sigma$	negl.	negl.	+0.010	−0.045	+0.056
Decay length bias	$\Delta\mathcal{A}$	negl.	+0.046	+0.082	−0.219	+0.186
	$\Delta\sigma$	negl.	−0.003	+0.020	+0.045	+0.008
Decay length resolution	$\Delta\mathcal{A}$	negl.	−0.010	+0.135	+0.359	+0.356
	$\Delta\sigma$	negl.	+0.020	+0.058	+0.185	+0.405
$\Delta\Gamma_s$	$\Delta\mathcal{A}$	−0.007	+0.025	+0.142	+0.187	+0.218
	$\Delta\sigma$	+0.003	−0.002	+0.018	−0.039	−0.023
Total systematic uncertainty		0.025	0.133	0.294	0.563	0.937

the input value, and in the data $\tau_{B_s^0} = (1.31 \pm 0.12)$ ps, (statistical uncertainty only), consistent with the present world average [1].

6 Inclusive semileptonic analysis

The third analysis [21] is based on an inclusive selection of semileptonic b-hadron decays.

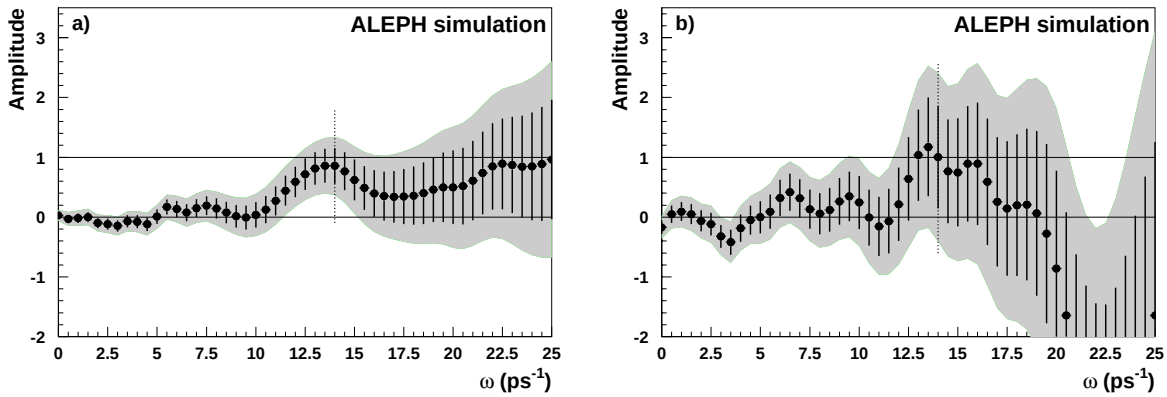

Figure 12: Amplitude spectrum for a) $D_s^- \ell^+$ simulated events, and b) the $D_s^- \ell^+$ selected sample in an unbiased $Z \to q\overline{q}$ sample corresponding to about twice the data statistics. The shaded area represents $\pm 1.645\,\sigma_{\mathcal{A}}^{\rm stat}$. In both cases the value of Δm_s chosen in the simulation $\omega = \Delta m_s^{\rm MC}$ is indicated with a dotted line.

6.1 Event Selection

Events well contained in the vertex detector acceptance are selected with the requirement that the thrust of the event satisfies $|\cos\theta_{\rm thrust}| < 0.85$. Events are divided into two hemispheres and clustered into jets with the JADE algorithm [15] using $y_{\rm cut} = 0.0044$. In the following, this jet definition is used to characterize events by their number of jets. Events are kept if they contain at least one lepton candidate, selected as in Ref. [19]. If more than one lepton is found in an event, that with the highest transverse momentum with respect to the closest jet is taken.

The decay length resolution is the limiting factor for the sensitivity of this analysis. Further selection criteria, based on the quality of the secondary vertex reconstruction, are applied to ensure a reliable estimate of the decay length uncertainty.

6.1.1 Vertexing

The procedure to reconstruct the b-hadron decay vertex closely follows that of Ref. [4]. A set of tracks is selected on the basis of kinematical properties and compatibility with an inclusively reconstructed tertiary vertex [13, 22]. These tracks are fitted to obtain an inclusive charmed-particle candidate (called the *D track* in the following). The D track is then fitted with the lepton to obtain the secondary vertex position.

Several new features are introduced to improve the decay length resolution.

- A cone-based jet is formed around the lepton candidate [23]. Its momentum direction is used as an improved estimator of the b hadron flight direction for events with three jets or more; in the case of two jet events, the thrust direction is taken instead as the best estimate of the b-hadron direction. A *B track* is constructed with this direction, forced to pass through the primary vertex. This track, with angular uncertainties parametrized from the simulation, is used in the secondary vertex fit together with the lepton and the D track. (Small correlations between these tracks are ignored.)

- For some candidates, the decay length resolution is improved by including leading photons

in the estimate of the D track flight direction. A cone-based jet is formed around the D track, and photons are selected in this jet. If more than one photon with energy greater than 1 GeV is found, that with the highest energy is added to the D track, if it forms an angle smaller than 16° with the jet direction and an invariant mass smaller than $1.8\,\mathrm{GeV}/c^2$ with the D track. The photon direction is determined with the D vertex as origin, instead of the primary vertex.

The b-hadron decay length is computed as the three-dimensional distance between the primary and secondary vertices. As the information on the b-hadron flight direction is already used in the secondary-vertex fit, the distance between production and decay vertices is not projected onto the b-jet direction, unlike in Ref. [4].

The use of the B track in the vertex fit gives an improvement on the $\mathrm{B_s^0}$ decay length resolution of up to 22%. The photon addition is found to be effective only for about 10% of the selected events.

Several vertex classes are defined based on characteristic parameters such as the reconstructed mass of the D track, the angle between the lepton and the D track, the number of tracks at the D vertex, and the χ^2 of both D and B vertices. Events not included in any of the classes are rejected. The vertexing and class selection have an efficiency of about 45% for $\mathrm{b} \to \ell$ decays and only about 28% for unbiased $\mathrm{Z} \to \mathrm{q\overline{q}}$ decays.

A bias correction is applied as a function of the measured decay length to obtain the final b-hadron decay length. Because of misidentified or missing particles at the D vertex, the decay length uncertainty provided by the fit is, in general, underestimated. The correction is parametrized as a function of the invariant mass of the D track and the reconstructed b-hadron decay length. Both corrections are extracted from simulated events in each of the vertex classes. The use of a parametrized correction for the pull distribution prevents the decay length uncertainty of the best reconstructed candidates from being degraded. The procedure is applied separately to direct and cascade decays, to account for different bias and pull corrections. This treatment constitutes a significant improvement compared to Ref. [4], in which a single, constant, correction factor was applied to the whole sample.

For illustration, the distribution of the decay length resolution for all vertex classes obtained with simulated signal events which pass the final selection (including the cuts discussed in Sections 6.1.2 and 6.1.3) is shown in Fig. 13a.

This vertexing algorithm, together with the lepton requirement, enhances the b content of the selected events. From an unbiased $\mathrm{q\overline{q}}$ sample of simulated events, those in the aforementioned vertex classes are found to be $\mathrm{b\overline{b}}$ with 83% probability. To further increase the purity, a dedicated b tagging is applied.

6.1.2 Selection of b events

Several variables which distinguish $\mathrm{Z} \to \mathrm{b\overline{b}}$ from other Z decays are combined with a neural network. The characteristic lifetime and mass of b hadrons is used as in Refs. [22, 24]. Because the candidate hemisphere contains a semileptonic decay, the properties of the lepton are also used. The hard fragmentation of b quarks and the mass of b hadrons result, respectively, in a large momentum and large transverse momentum of the primary lepton compared to that of leptons produced in the decay of light-quark hadrons. The distribution of the combined variable

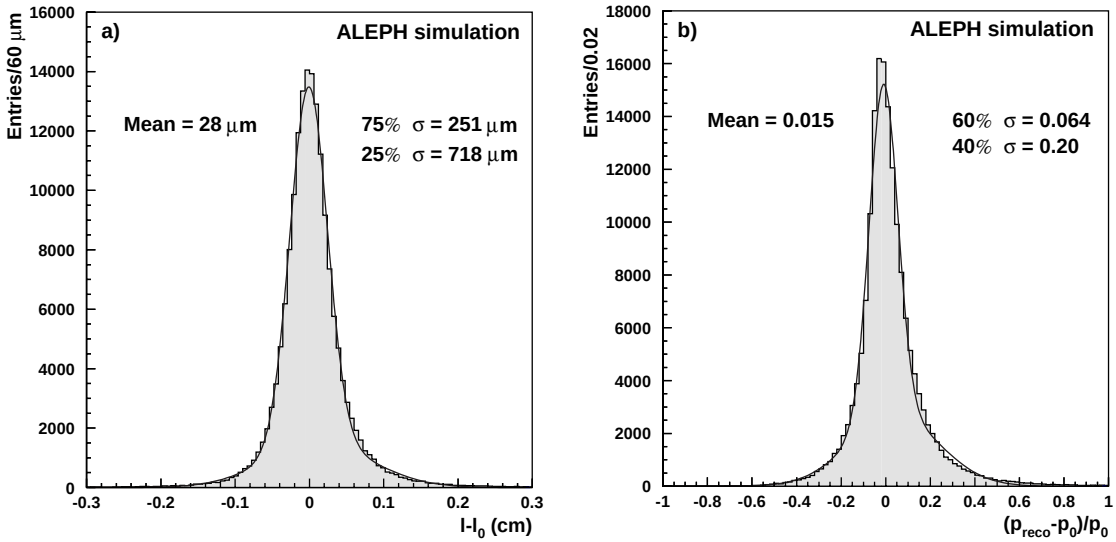

Figure 13: a) Decay length resolution for selected $B_s^0 \to \ell$ simulated events, and b) relative momentum resolution for selected $B_s^0 \to \ell$ simulated events. In both cases, the curve is the result of a fit with two Gaussian functions, with relative fractions and widths as indicated.

N_b for events passing the vertex selection is displayed in Fig. 14a; the discrimination power is apparent, as well as the agreement between the data and the simulated $Z \to q\overline{q}$ events.

Events with very low probability of being a $Z \to b\overline{b}$ decay are rejected with a cut at $N_b > 0$. The sample selected has an average b-hadron purity increased to 98%, for a 10% loss in efficiency. The average sample composition in $Z \to b\overline{b}$ or $Z \to u\overline{u}$, $d\overline{d}$, $s\overline{s}$, $c\overline{c}$ is parametrized with simulated events as a function of the combined b-tagging variable. An event-by-event signal probability is defined from this parametrization and is then used in the oscillation fit.

6.1.3 Selection of $b \to \ell$ decays

After the vertex selection and the b tag cut, the fraction of direct $b \to \ell$ decays is on average 67%, whereas about 23% of hemispheres contain cascade decays ($b \to c \to \ell$) in which the charge correlation between the b quark and the lepton is reversed. In the analysis of Ref. [4], a cut on the transverse momentum of the lepton with respect to the b jet was applied to reject cascade decays. Here, the lepton transverse momentum is further combined with other discriminant variables in a neural network to get an optimal separation between direct and cascade semileptonic b decays.

The following properties are exploited in the neural network. The lepton momentum and transverse momentum spectra, as well as the neutrino energy spectrum, are expected to be harder for direct $b \to \ell$ decays than for other decays. Some properties of the b-hadron jet which contains the lepton candidate are also considered, as $b \to \ell$ and $b \to c \to \ell$ decays lead to significantly different jet topologies. The boost of the b hadron, however, tends to dilute some of these differences; it is therefore more appropriate to study the separation in the rest frame of the lepton and the D track. Four topological variables are defined in that rest frame, as described in Ref. [25]. Finally, the signed impact parameter significance of the lepton with respect to the D vertex is computed, with the sign given by the D track flight direction. The lepton is expected to be found upstream of the D vertex for $b \to \ell$ decays, and therefore to have

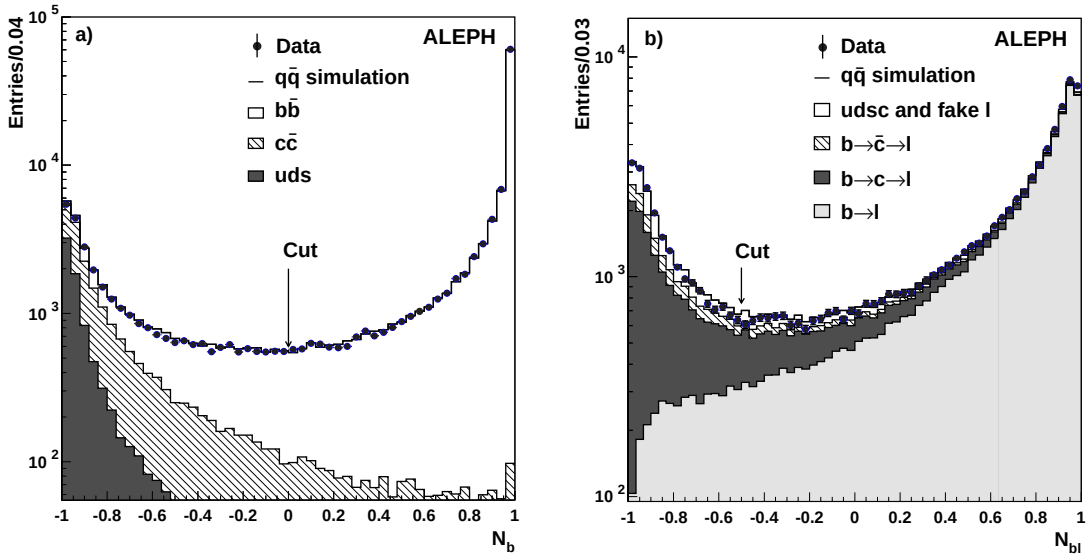

Figure 14: a) The b-tagging variable distribution for events selected with a lepton and a reconstructed B vertex. The label "uds" stands for $Z \to u\overline{u}$, $d\overline{d}$, $s\overline{s}$; b) The $b \to \ell$ tagging variable distribution for hemispheres selected with the b-tagging cut in addition. The label "udsc" stands for $Z \to u\overline{u}$, $d\overline{d}$, $s\overline{s}$, $c\overline{c}$ and "fake ℓ" corresponds to hemispheres in which the lepton candidate is either not a lepton or a lepton from a light-quark decay.

a negative impact parameter significance.

The distribution of the combined variable $N_{\rm bl}$ is shown in Fig. 14b for simulated and data events. A clear separation between direct decays with $N_{\rm bl}$ close to unity with respect to the other decays is observed. Candidates with $N_{\rm bl} < -0.5$ are rejected. The position of this cut is optimized to reject candidates with a probability of getting the correct sign from the lepton smaller than 0.5. The final-state tag is defined by the sign of the lepton. The mistag probability is parametrized as a function of $N_{\rm bl}$ and hence used event by event.

6.1.4 Final sample composition

The final event sample is defined by the lepton selection, the vertex selection, the b-hadron selection, and the $b \to \ell$ decays selection. After all these criteria are applied, 74 026 candidates are selected in the data, to be compared with 33 023 in Ref. [4]. The sample composition is evaluated from simulated $Z \to q\overline{q}$ events, $(98.6 \pm 0.4)\%$ $b\overline{b}$, $(1.15 \pm 0.03)\%$ $c\overline{c}$, and $(0.25 \pm 0.02)\%$ light-quark pairs. On average 87% of the $b\overline{b}$ events contain direct semileptonic decays; the fraction increases to 94% if only the 50 000 candidates most likely to be $b \to \ell$ are considered.

6.2 Proper-time reconstruction

As explained in Section 3.1, the proper time of each selected event is reconstructed from its decay length, measured as described in Section 6.1.1, the momentum of the b hadron, and the nominal B_s^0 mass [1]. The estimate of the b-hadron momentum is performed as follows. The energy of the D track, $E_{\rm D}$, is estimated [4] by the energy of a "nucleated" jet clustered around

the charged particles at the D vertex until a mass of $2.7\,\mathrm{GeV}/c^2$ is reached, excluding particles with momentum less than $0.5\,\mathrm{GeV}/c$. The energy of the neutrino, E_ν, is determined as in Section 5.2. These two ingredients, supplemented by the energy of the lepton candidate, E_ℓ, are used to compute the b-hadron momentum as $p = \sqrt{(E_\mathrm{D} + E_\nu + E_\ell)^2 - m^2}$.

The reconstructed momentum is found to have a positive bias with respect to the true momentum. This bias increases with the measured neutrino energy, because the estimate of the D track energy is designed to optimize the average b-hadron momentum resolution independently of the neutrino energy. A correction accounts for this effect in each vertex class.

The distribution of $(p - p_0)/p_0$ is shown in Fig. 13b for all selected candidates in a sample of simulated $\mathrm{B_s^0} \to \ell$ decays, of which 60% are found in a core with 6.4% relative momentum resolution, and 40% in a tail with 20% resolution. (These average values are not used for the oscillation fit.) In each vertex class, candidates are binned in lepton momentum. A fit with the sum of two Gaussian functions is performed to the relative momentum resolution distribution in each of these bins. The widths and mean values of these Gaussian functions are parametrized with a linear dependence on the lepton momentum. For each candidate, the corresponding relative width $\delta^i_{p_1} (\equiv \sigma^i_{p_1}/p)$ and $\delta^i_{p_2}$, and relative weights $f^i_{p_1}$ and $f^i_{p_2}$ are used in the oscillation fit (Eq. 5).

6.3 Initial-state tag

The method to tag the initial $\mathrm{B_s^0}$ flavour described in Section 3.2.2 is used here with some modifications in the definition of the same-side variables. In the inclusive semileptonic analysis, the charged particles originating from the $\mathrm{B_s^0}$ decay are not fully identified. The charge estimators described in Section 3.2.2 cannot therefore be constructed in the same manner.

All charge estimators are computed only with particles inside the wide b jet, defined in Section 3.2.2. A neural network is trained on the selected hemispheres to separate tracks originating from the primary and the secondary vertices. A weight, which gives the probability to come from the secondary vertex, is computed for each track in the wide b jet and used to construct charge variables.

The charge variables are (*i*) three primary vertex charges ($\kappa = 0,\ 0.6,\ 1$) with all charged particles in the wide b jet weighted according to their probability to originate from the primary vertex; (*ii*) two primary vertex charges ($\kappa = 0,\ 0.3$) with all charged particles in the wide b jet except those of the D vertex; and (*iii*) a charged fragmentation kaon estimator, obtained from a neural network similar to that in Section 3.2.2. (Each charged particle is weighted with its probability to originate from the primary vertex and the training is performed to identify fragmentation kaons in $\mathrm{B_s^0} \to \ell$ decays.)

The initial-state tag determination then proceeds as described in Section 3.2.2.

6.4 Determination of the purity

The $\mathrm{B_s^0}$ signal decays are distinguished from other b hadrons in two ways. First, variables related to the electric charge and the charged particle multiplicity of the tertiary vertex distinguish charged from neutral b hadrons. The presence of kaons (charged and neutral) among fragmentation and decay particles also distinguish $\mathrm{B_s^0}$ decays from the other b hadrons. For the charged decay kaons, the charge correlation with the lepton candidate is the best discriminant.

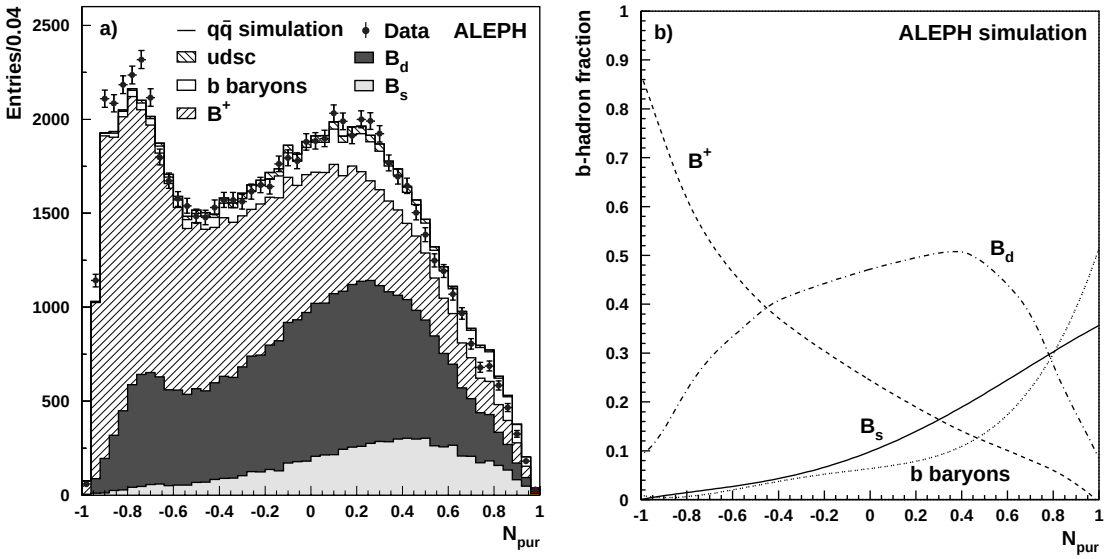

Figure 15: a) Distribution of the B_s^0 purity variable. The B_s^0 decays are concentrated at high values of $N_{\rm pur}$ and B^+ decays at low values. b) Fraction of each b-hadron species as a function of the $N_{\rm pur}$ variable.

Discriminant variables sensitive to these characteristics are identified and combined with a neural network. Simulated events are used to turn the combined variable $N_{\rm pur}$ into a probability for each candidate to be a B_s^0, B^0, B^+ or b-baryon decay.

A deficit of simulated decays in the region mostly populated by B^+ mesons is observed. All input charge estimators used to separate neutral from charged b hadrons show a similar disagreement. The tertiary vertex charge variable, if used to fit the amount of charged and neutral b hadrons, indicates that the selected data sample contains 8% more charged b decays than the simulation. When this correction is applied to simulated decays, the variables which distinguish charged from neutral b hadrons show a significantly improved agreement. The corrected distribution of $N_{\rm pur}$ (Fig. 15a) still displays some discrepancy, although reduced by more than a factor of two. This residual discrepancy is attributed to differences in shape for the variables that distinguish B_s^0 decays from the other neutral b hadrons. The effect of a difference in shape on the event-by-event estimated B_s^0 purity is smaller than the effect of a bias in the selection efficiency. A possible systematic effect due to the residual discrepancy is estimated by removing and applying twice the weights which readjust the charged-to-neutral ratio (Section 6.5.1).

The purity of each b-hadron species is shown as a function of the discriminating variable in Fig. 15b. For 17% of the candidates in the selected sample ($N_{\rm pur} > 0.4$), the B_s^0 purity is estimated to be 20% or higher. The effective B_s^0 purity of the whole sample is evaluated to be about 12.5%, to be compared with the average purity of about 10%.

6.5 The B_s^0 oscillations results

The likelihood functions for the four b-hadron components (B_s^0, B^0, B^+ and b baryons) are obtained analytically as explained in Section 3.4. The non-b background proper-time

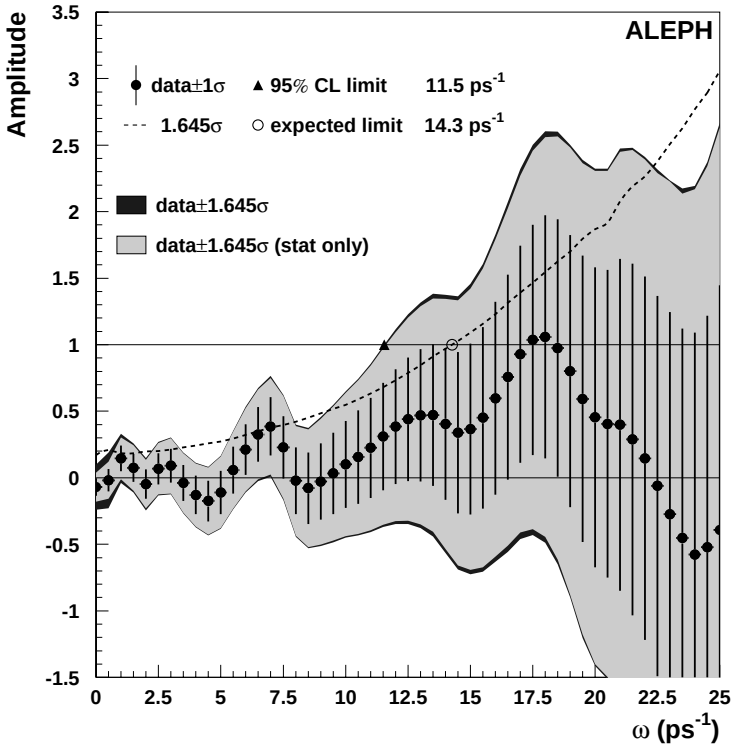

Figure 16: Fitted amplitude spectrum as a function of the test frequency for the inclusive semileptonic sample.

distribution is taken from the simulation.

The probability density functions which describe the proper-time distributions of the four b-hadron species (Eq. 4) are folded with a resolution function (Eq. 5) and with the proper-time reconstruction efficiency. The selection cuts which define the vertex classes (Section 6.1.1) are designed to reduce the fraction of fragmentation particles assigned to the D vertex. Consequently they cause a loss of efficiency at small true proper times. Similarly, at large proper times the efficiency also decreases due to the quality cuts on the selected tracks. The efficiencies are parametrized separately for each b-hadron component and each vertex class. They are independent of whether the B_s^0 candidate is tagged as mixed or unmixed.

The proper-time distributions expected for light-quark and charm hadrons are in principle expected to differ due to their different characteristic lifetimes. However, the bias introduced by the inclusive semileptonic event selection on the light-quark and charm events is such that the two distributions are found to be very similar. A single function is parametrized from the simulation for the non-b background component. This function, which includes the resolution and reconstruction inefficiency effects by construction, is used for the likelihood fit.

An amplitude fit is performed as a function of the oscillation frequency, and the result is shown in Fig. 16 with statistical and systematic uncertainties. All frequency values below $11.5\,\mathrm{ps}^{-1}$ are excluded at 95% C.L., while the expected limit is $14.3\,\mathrm{ps}^{-1}$.

6.5.1 Systematic Uncertainties

The input parameter uncertainties are accounted for as explained in Section 3.4. All systematic uncertainties studied are summarized in Table 8.

Table 8: Systematic uncertainties on the amplitude at different oscillation frequency values compared to the statistical uncertainty, for the inclusive semileptonic selection. The shift of both the measured amplitude, $\Delta\mathcal{A}$, and of its statistical uncertainty, $\Delta\sigma$, are listed for each parameter, signed according to their change when the parameter is increased.

Oscillation frequency		0 ps^{-1}	10 ps^{-1}	15 ps^{-1}	20 ps^{-1}	25 ps^{-1}
Statistical uncertainty		0.066	0.327	0.642	1.126	1.837
Momentum resolution	$\Delta\mathcal{A}$	−0.008	+0.031	+0.073	+0.092	−0.107
	$\Delta\sigma$	negl.	+0.024	+0.047	+0.085	+0.161
Decay length resolution	$\Delta\mathcal{A}$	−0.001	+0.006	+0.059	+0.047	−0.120
	$\Delta\sigma$	negl.	+0.010	+0.033	+0.066	+0.093
Mistag	$\Delta\mathcal{A}$	−0.004	+0.005	+0.021	+0.019	−0.026
	$\Delta\sigma$	+0.003	+0.017	+0.035	+0.062	+0.107
$\mathrm{B_s^0}$ purity	$\Delta\mathcal{A}$	−0.024	−0.003	−0.060	−0.033	+0.067
	$\Delta\sigma$	−0.003	−0.013	−0.028	−0.050	−0.096
f_s	$\Delta\mathcal{A}$	+0.070	−0.054	−0.135	−0.096	−0.100
	$\Delta\sigma$	−0.007	−0.032	−0.064	−0.113	−0.185
$\tau_{\mathrm{B_s^0}}$	$\Delta\mathcal{A}$	−0.006	+0.008	+0.022	+0.005	+0.025
	$\Delta\sigma$	negl.	+0.005	+0.013	+0.020	+0.004
$\tau_{\mathrm{B^0}}$	$\Delta\mathcal{A}$	+0.005	−0.001	−0.003	−0.001	−0.009
	$\Delta\sigma$	negl.	−0.001	−0.003	−0.002	+0.015
$\tau_{\mathrm{B^+}}$	$\Delta\mathcal{A}$	−0.009	+0.006	+0.011	+0.031	+0.044
	$\Delta\sigma$	negl.	negl.	−0.002	−0.003	+0.010
$\tau_{\mathrm{b-baryon}}$	$\Delta\mathcal{A}$	−0.006	−0.004	−0.008	−0.007	−0.013
	$\Delta\sigma$	negl.	−0.001	−0.003	−0.010	−0.002
$\mathrm{b} \to \ell$	$\Delta\mathcal{A}$	−0.004	+0.003	+0.004	+0.007	+0.012
	$\Delta\sigma$	negl.	negl.	negl.	−0.001	+0.005
$\mathrm{b} \to \mathrm{c} \to \ell$	$\Delta\mathcal{A}$	−0.007	+0.005	+0.006	+0.008	+0.023
	$\Delta\sigma$	negl.	−0.001	−0.001	+0.001	−0.018
$\mathrm{b} \to \overline{\mathrm{c}} \to \ell$	$\Delta\mathcal{A}$	+0.007	−0.006	−0.006	−0.009	−0.026
	$\Delta\sigma$	negl.	+0.001	+0.001	+0.004	+0.037
Δm_d	$\Delta\mathcal{A}$	+0.022	negl.	negl.	+0.002	−0.001
	$\Delta\sigma$	negl.	negl.	negl.	+0.012	−0.007
Efficiency	$\Delta\mathcal{A}$	−0.008	−0.019	+0.013	+0.052	+0.137
	$\Delta\sigma$	negl.	+0.011	+0.027	+0.069	+0.097
Non-b background	$\Delta\mathcal{A}$	+0.007	−0.013	−0.041	−0.041	−0.085
	$\Delta\sigma$	negl.	+0.002	+0.009	+0.021	+0.442
$\Delta\Gamma_\mathrm{s}$	$\Delta\mathcal{A}$	+0.005	negl.	negl.	+0.003	−0.005
	$\Delta\sigma$	+0.001	+0.001	negl.	negl.	+0.008
Total systematic uncertainty		0.079	0.067	0.165	0.143	0.283

The momentum resolution is obtained from simulated events, as described in Section 6.2. The candidate events in the semi-exclusive selection of semileptonic $\mathrm{B^0}$ and $\mathrm{B^+}$ decays described in Ref. [20] are used to check the agreement between data and simulation for the b-hadron momentum reconstruction. The momentum of each b-meson candidate is reconstructed (i) with

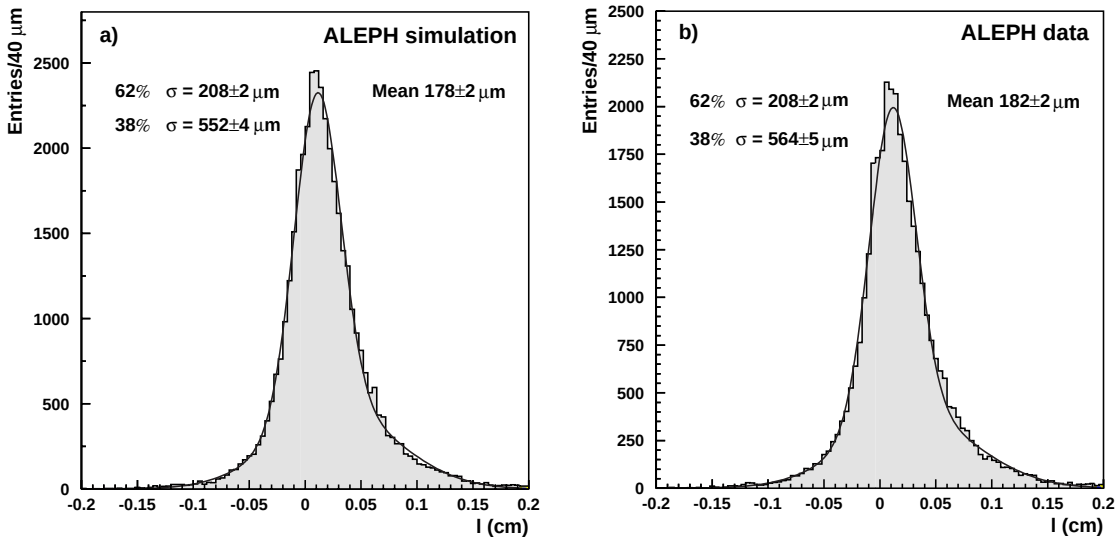

Figure 17: Distribution of the distance between the primary vertex reconstructed with the secondary vertexing algorithm (Section 6.1.1) and the standard ALEPH algorithm [7], a) for the simulation, and b) for the data.

the method used in the inclusive semileptonic analysis and (*ii*) more accurately from the identified decay products. (Only the reconstruction of the D track momentum is different in the two cases.) The difference between these two estimates of the b-hadron momentum is compared in data and simulation. No significant bias is observed, but a 10% (35%) difference of the core (tail) resolution is observed and used to estimate the systematic uncertainty on the momentum resolution. The uncertainty on the estimate of the neutrino energy is less than 50 MeV [20] and its effect is therefore neglected here.

For each candidate, the decay length is obtained from the B-vertex fit and from the bias correction, the decay length uncertainty from the B-vertex fit and from the pull correction. Both corrections are obtained from simulated events. They are therefore reliable only to the extent that the vertexing algorithm has the same performance on data and simulation. To check this point, a specific analysis is performed. Events arising from Z decays into light quarks are selected and the secondary vertexing algorithm explained in Section 6.1.1 is used on such events to reconstruct the primary vertex. The "decay length" is defined as the distance between the primary vertex reconstructed with the vertexing algorithm and that with the standard method [7]. The "decay length" distribution is used to compare the performance of the vertexing algorithm in data and simulation, and the two distributions are found to agree, as shown in Fig. 17. This indicates that the vertexing algorithm has the same performance on data and simulation, at least for events without lifetime. The check is, however, not sensitive to the effect of track misassignment to the D track. The same events used to check the momentum reconstruction are used to investigate a possible related effect. The decay length obtained from the full reconstruction is compared to that obtained with the algorithm used in this analysis. No significant bias between data and simulation is observed in the distribution of the difference between the two decay length estimates. However a 3% difference in the resolution is observed

Table 9: Input parameters to the B_s^0 oscillation fit, in the inclusive semileptonic analysis.

f_s	(10.7 ± 1.4) %	[1]
$\tau_{B_s^0}$	(1.464 ± 0.057) ps	[1]
τ_{B^0}	(1.540 ± 0.024) ps	[1]
τ_{B^+}	(1.655 ± 0.027) ps	[1]
$\tau_{b-baryon}$	(1.208 ± 0.051) ps	[1]
$BR(b \to \ell)$	(10.67 ± 0.21) %	[26]
$BR(b \to c \to \ell)$	(8.07 ± 0.17) %	[26]
$BR(b \to \overline{c} \to \ell)$	$(1.62^{+0.44}_{-0.36})$ %	[27]
Δm_d	(0.476 ± 0.012) ps^{-1}	[1]

and is used to estimate the systematic uncertainty on the decay length resolution.

The dependence of the mistag probability on the initial-state tag variable is found to be linear with no offset, for signal events. For systematic studies the slope is varied by 10% as in Ref. [13].

As explained in Section 6.4, a discrepancy between data and simulation in the B_s^0 purity variable distribution is observed. Weights are applied to simulated events to increase by 8% the amount of charged b hadrons and improve the agreement with the data. These weights are removed (or applied twice) for the systematic uncertainty evaluation.

The relevant input parameters for the B_s^0 oscillation fit, considered as possible sources of systematic uncertainties, are shown with their uncertainties in Table 9. The fraction of B_s^0 mesons in an unbiased b-hadron sample, f_s, gives one of the largest effects.

A variation of Δm_d only affects the amplitude spectrum in the frequency region $\omega \sim \Delta m_d$. It is one of the dominant systematic effects at low frequency, but it is negligible at the frequency range of interest.

The reconstruction efficiency was obtained from the simulation as a function of proper time for each b-hadron species and each vertex class. An amplitude fit is performed with a uniform efficiency to check that the effect on the Δm_s analysis is small.

The uncertainty on the amount of charm and light quark background is estimated to be 20% and 30%, respectively, following Ref. [24]. The amplitude fit is performed again with a likelihood function which takes into account a nonzero value of $\Delta\Gamma_s$ (Section 4.8.1).

6.5.2 Checks

Several checks of the analysis method and of the sample description are performed using the simulation, and with the data sample when possible.

A first check is done with the simulated B_s^0 signal. A likelihood fit for the oscillation frequency is performed on the selected B_s^0 candidates from the $Z \to q\overline{q}$ simulated sample. The result obtained is $\Delta m_s = (13.8 \pm 0.3)\,\text{ps}^{-1}$ in agreement with the input value of $14\,\text{ps}^{-1}$. The corresponding amplitude scan is shown in Fig. 18a, the fitted amplitude is compatible with zero before the true oscillation frequency and with unity at $\Delta m_s^{MC} = 14\,\text{ps}^{-1}$.

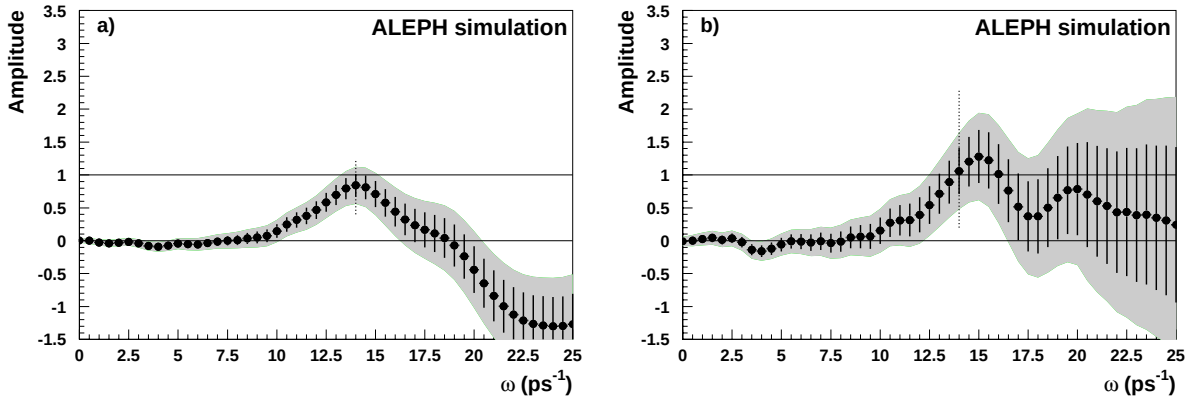

Figure 18: Amplitude spectrum for a) a sample of B_s^0 simulated events, and b) a sample of selected $Z \to q\overline{q}$ simulated events. The statistics of this sample are a factor 1.6 larger than that of the data sample. The shaded area represents $\pm 1.645\,\sigma_{\mathcal{A}}^{\rm stat}$. In both cases the value of Δm_s chosen in the simulation $\omega = \Delta m_s^{\rm MC}$ is indicated with a dotted line.

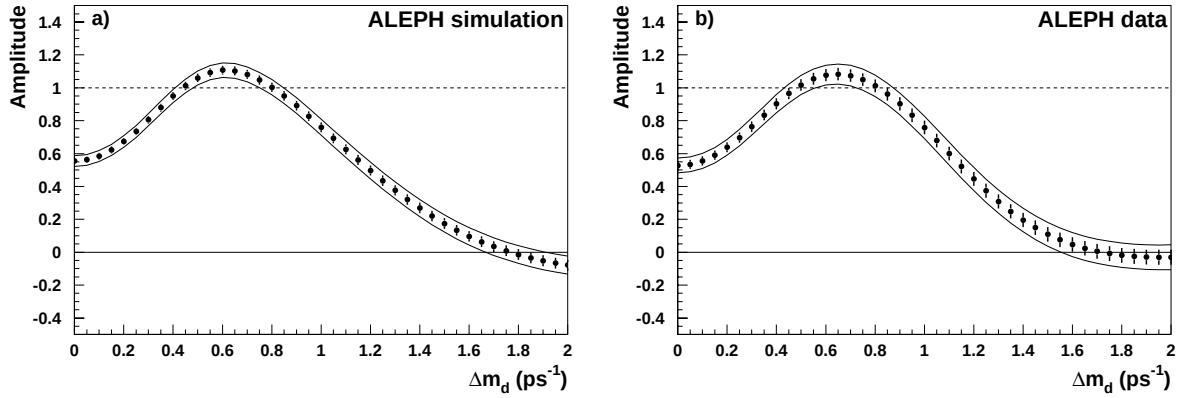

Figure 19: Amplitude spectrum for B^0 oscillations in a) the simulation and b) the data. The envelope represents $\pm 1.645\,\sigma_{\mathcal{A}}^{\rm stat}$.

The corresponding study is made for all vertex classes separately with similar results. The fit with the complete $Z \to q\overline{q}$ simulated sample gives $\Delta m_s = (14.6 \pm 0.7)\,{\rm ps}^{-1}$, with a significance of over three standard deviations. The corresponding amplitude spectrum is shown in Fig. 18b, in agreement with the expectation.

Although the description of the data sample is optimized for B_s^0 oscillation studies, other parameters can be measured as a further check of consistency. In particular, a fit to the B^0 oscillation frequency Δm_d is performed both in the $Z \to q\overline{q}$ simulated sample and in the data. The corresponding amplitude spectra are shown in Fig. 19a and Fig. 19b.

A careful measurement of the B^0 oscillation frequency is not attempted here because the selection is not optimized for such a measurement. The amplitude spectra are similar in data and simulation. However, the likelihood maximum is about 10% too high, $\Delta m_d = 0.53\,{\rm ps}^{-1}$ in the simulation ($\Delta m_d^{\rm MC} = 0.47\,{\rm ps}^{-1}$) and $\Delta m_d = 0.55\,{\rm ps}^{-1}$ in the data. The difference with respect to the true value is accounted for by the systematic uncertainties. The effect of the

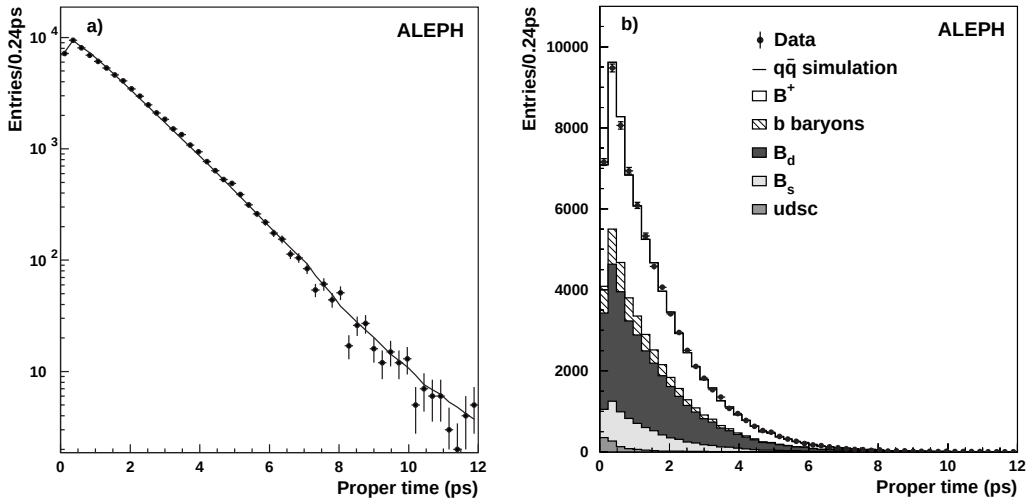

Figure 20: Reconstructed proper-time distributions of the selected candidates in the data; a) the curve is the result of the likelihood fit, and b) a comparison with the simulated sample.

momentum resolution, the proper-time efficiency parametrization and the flavour tagging are evaluated and result in about a 15% uncertainty on the fitted value of $\Delta m_{\rm d}$.

A fit for the average b-hadron lifetime of the sample is performed both on the simulation and on the data. The results obtained are $\tau_{\rm ave} = (1.556 \pm 0.008)$ ps in the simulation, consistent with the input values of the b-hadron lifetimes and production fractions, and $\tau_{\rm ave} = (1.54 \pm 0.01)$ ps in the data (statistical uncertainty only), in agreement with the present world average [1]. The fitted proper-time likelihood function is shown superimposed on the data in Fig. 20a. In Fig. 20b, the proper-time distribution in the data is compared to that in the simulation, and good agreement is observed.

7 Combined results

The three analyses presented in this paper are combined. A previously published ALEPH analysis [28] based on fully reconstructed $\rm D_s^-$ candidates paired with an oppositely charged hadron is not included in the combination as it is substantially less sensitive than the analyses presented here and has some statistical overlap with the fully reconstructed $\rm B_s^0$ analysis.

Some of the events selected in the $\rm D_s^- \ell^+$ sample are also selected in the inclusive semileptonic sample. To avoid any statistical correlation between the two analyses, about 150 events in common are removed from the inclusive semileptonic event sample before the combination is performed. Systematic uncertainties are found not to be a limitation for any of the three analyses, nor for their combination.

The combination of the amplitude spectra of the three analyses is displayed in Fig. 21. A lower limit on the $\rm B_s^0$ oscillation frequency of $\Delta m_{\rm s} > 10.9$ ps^{-1} at 95% C.L. is obtained, substantially lower than the expected limit of 15.7 ps^{-1}. The negative log-likelihood curves with respect to infinity are shown in Fig. 22 for each of the analyses, and the combination. No significant minimum is observed.

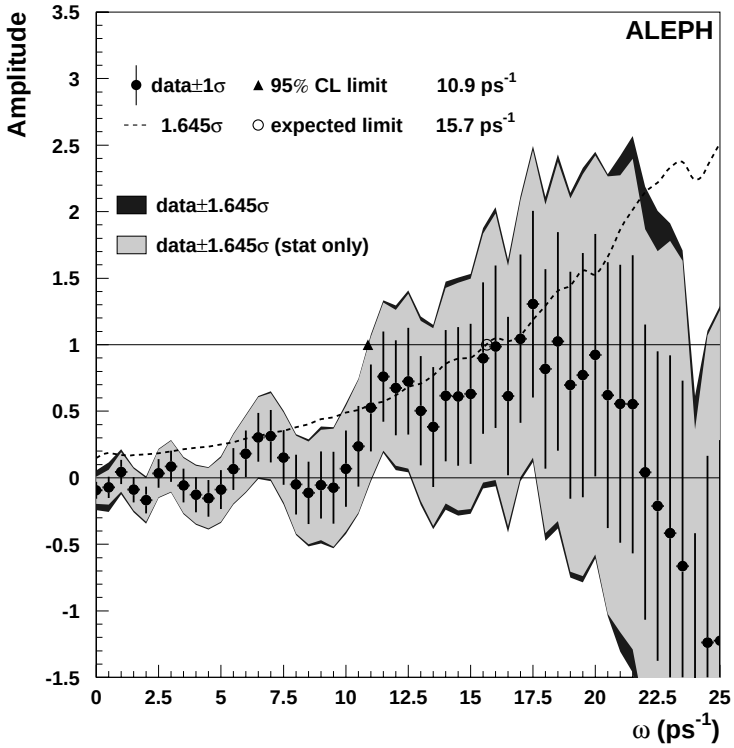

Figure 21: ALEPH combined amplitude spectrum.

8 Conclusion

An improved search for B_s^0 oscillations has been performed with the data sample collected by ALEPH during the first phase of LEP. Three complementary analyses have been presented. An analysis based on fully reconstructed B_s^0 decays is performed for the first time in ALEPH. The other two analyses, based on semileptonic decays, improve significantly upon earlier results. The three analyses are combined to give the final ALEPH result. The expected limit, $15.7\,\mathrm{ps}^{-1}$, has substantially improved since the last publication [4], when it was $10.6\,\mathrm{ps}^{-1}$. It is the highest that has yet been achieved in a single experiment [29]. The observed limit is $\Delta m_s > 10.9\,\mathrm{ps}^{-1}$ at 95% C.L., significantly lower than the expected limit. The difference between the expected and observed limits is due to positive measured amplitudes at frequencies close to the expected limit, suggesting that the signal may lie in that frequency region.

Acknowledgements

We wish to thank our colleagues from the accelerator divisions for the successful operation of LEP. It is also a pleasure to thank the technical personnel of the collaborating institutions for their support in constructing and maintaining the ALEPH experiment. Those of us from non-member states thank CERN for its hospitality.

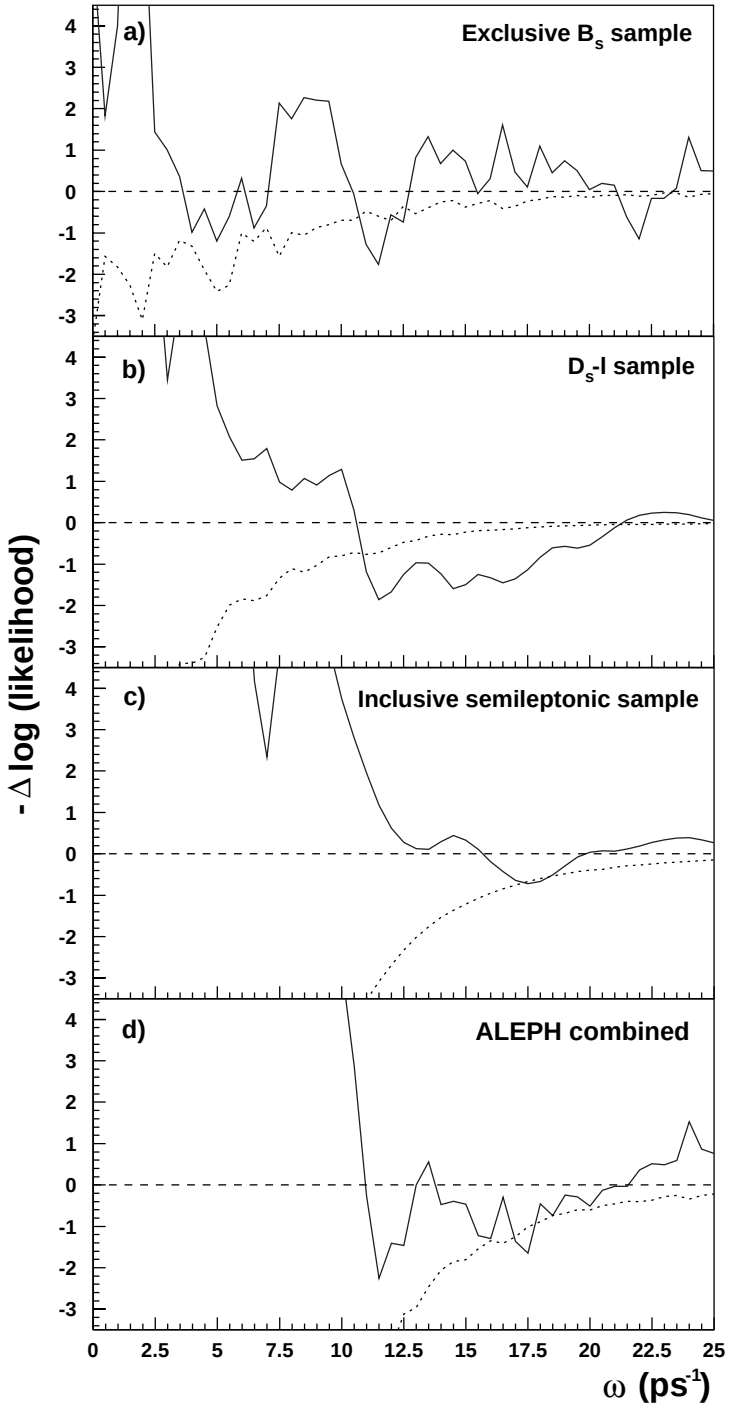

Figure 22: Negative log-likelihood relative to the value at infinite frequency a-c) for the three analyses, and d) for the ALEPH combination. The dotted curves give the expected likelihood depth at each frequency for $\omega = \Delta m_{\rm s}$.

References

[1] The Particle Data Group, *Review of Particle Physics*, Eur. Phys. J. **C15** (2000) 1.

[2] C. Weiser, *Studies of B_s oscillations at LEP*, in Proceedings of EPS International Conference on High Energy Physics, Budapest 2001, `PrHEP-hep2001/095`.

[3] The ALEPH Collaboration, *Study of the $B_s^0 - \overline{B}_s^0$ oscillation frequency using $D_s^- \ell^+$ combinations in Z decays*, Phys. Lett. **B377** (1996) 205.

[4] The ALEPH Collaboration, *Search for B_s^0 oscillations using inclusive lepton events*, Eur. Phys. J. **C7** (1999) 553.

[5] The ALEPH Collaboration, *ALEPH: a detector for electron-positron annihilations at LEP*, Nucl. Instrum. and Methods **A294** (1990) 121.

[6] The ALEPH Collaboration, *Performance of the ALEPH detector at LEP*, Nucl. Instrum. and Methods **A360** (1995) 481.

[7] The ALEPH Collaboration, *Measurement of the $\overline{B}^0$ and B^- Meson Lifetimes*, Phys. Lett. **B492** (2000) 275.

[8] The ALEPH Collaboration, *Measurement of the Z Resonance Parameters at LEP*, Eur. Phys. J. **C14** (2000) 1.

[9] "GEANT Detector Description and Simulation Tool", CERN Program Library, CERN-W5013, (1993).

[10] T. Sjöstrand and M. Bengtsson, *The LUND Monte Carlo for jet fragmentation and e^+e^- physics -JETSET version 6.3- and update*, Comput. Phys. Commun. **43** (1987) 367.

[11] The ALEPH Collaboration, *Studies of Quantum Chromodynamics with the ALEPH Detector*, Phys. Rep. **294** (1998) 1.

[12] The ALEPH Collaboration, *Heavy quark tagging with leptons in the ALEPH detector*, Z. Phys. **C62** (1994) 179.

[13] The ALEPH Collaboration, *Study of the CP asymmetry of $B^0 \to \psi K_S^0$ decays in ALEPH*, Phys. Lett. **B492** (2000) 259.

[14] The ALEPH Collaboration, *Measurement of A_{FB}^b using inclusive b-hadron decays*, CERN EP/2001-047, to be published in Eur. Phys. J. **C**.

[15] The JADE Collaboration, *Experimental studies on multijet production in e^+e^- annihilations at PETRA energies*, Z. Phys. **C33** (1986) 23.

[16] H.-G. Moser and A. Roussarie, *Mathematical methods for $B^0 - \overline{B}^0$ oscillation analyses*, Nucl. Instrum. and Methods **A384** (1997) 491.

[17] D. Abbaneo and G. Boix, *The B_s^0 oscillation amplitude analysis*, Journal of High Energy Physics **JHEP08** (1999) 004.

[18] ALEPH, CDF, DELPHI, L3, OPAL, SLD Collaborations, *Combined results on b-hadron production rates and decay properties*, CERN EP/2001-050.

[19] The ALEPH Collaboration, *Inclusive semileptonic branching ratios of b hadrons produced in Z decays*, CERN EP/2001-057, to be published in Eur. Phys. J. **C**.

[20] The ALEPH Collaboration, *Study of the fragmentation of b quarks into B mesons at the Z peak*, Phys. Lett. **B512** (2001) 30.

[21] G. Boix, *Study of B_s oscillations with the ALEPH detector at LEP*, Ph.D. thesis, Universitat Autònoma de Barcelona, 2001.

[22] The ALEPH Collaboration, *An investigation of B_d^0 and B_s^0 oscillation*, Phys. Lett. **B322** (1994) 441.

[23] The OPAL Collaboration, *QCD studies using a cone-based jet algorithm for e^+e^- collisions at LEP*, Z. Phys. **C63** (1994) 197.

[24] The ALEPH Collaboration, *A measurement of R_b using a lifetime-mass tag*, Phys. Lett. **B401** (1997) 150.

[25] The ALEPH Collaboration, *Measurement of the Forward-Backward Asymmetries in $Z \to b\bar{b}$ and $Z \to c\bar{c}$ Decays with Leptons*, CERN EP/2001-097, submitted to Eur. Phys. J. **C**.

[26] F. Palla, *Semileptonic B decays and CKM elements at LEP*, in Proceedings of EPS International Conference on High Energy Physics, Budapest 2001, `PrHEP-hep2001/077`.

[27] The ALEPH, DELPHI, L3, and OPAL Collaborations, the LEP Electroweak Working Group and the SLD Electroweak and Heavy Flavour Groups, *Precision Electroweak Measurements on the Z resonance*, Physics Report in preparation.

[28] The ALEPH Collaboration, *Study of B_s^0 oscillations and lifetime using fully reconstructed D_s^- decays*, Eur. Phys. J. **C4** (1998) 367.

[29] The DELPHI Collaboration, *Study of $B_s^0 - \overline{B}_s^0$ oscillations and B_s^0 lifetimes using hadronic decays of B_s^0 mesons*, Eur. Phys. J. **C18** (2000) 229.
The CDF Collaboration, *A search for $B_s^0 - \overline{B}_s^0$ oscillations using the semileptonic decay $B_s^0 \to \phi\, \ell^+\, X\, \nu$*, Phys. Rev. Lett. **82** (1999) 3576.
The OPAL Collaboration, *A Study of B_s meson oscillation using D_s-lepton Correlations*, Eur. Phys. J. **C19** (2001) 241.